



Title	Catalytic activities of titania-supported nickel for carbon-dioxide methanation
Author(s)	Unwiset, Preeya; Chanapatttharapol, Kingkaew Chayakul; Kidkhunthod, Pinit et al.
Citation	Chemical Engineering Science, 228, 115955 <a href="https://doi.org/10.1016/j.ces.2020.115955">https://doi.org/10.1016/j.ces.2020.115955</a>
Issue Date	2020-12-31
Doc URL	<a href="https://hdl.handle.net/2115/87838">https://hdl.handle.net/2115/87838</a>
Rights	© 2020. This manuscript version is made available under the CC-BY-NC-ND 4.0 license <a href="http://creativecommons.org/licenses/by-nc-nd/4.0/">http://creativecommons.org/licenses/by-nc-nd/4.0/</a>
Rights(URL)	<a href="https://creativecommons.org/licenses/by-nc-nd/4.0/">https://creativecommons.org/licenses/by-nc-nd/4.0/</a>
Type	journal article
File Information	Ni-PREEY_011.pdf



# Catalytic activities of titania-supported nickel for carbon-dioxide methanation

Preeya Unwiset<sup>a</sup>, Kingkaew Chayakul Chanapattharapol<sup>a\*</sup>,

Pinit Kidkhunthod<sup>b</sup>, Yingyot Poo-arporn<sup>b</sup>, Bunsho Ohtani<sup>c</sup>

<sup>a</sup>Materials Chemistry Research Center, Department of Chemistry and Center of Excellence for Innovation in Chemistry, Faculty of science, Khon Kaen University, Khon Kaen, 40002, Thailand

<sup>b</sup>Synchrotron Light Research Institute, 111 University Avenue, Muang District, Nakhon Ratchasima, 30000, Thailand

<sup>c</sup>Institute for Catalysis, Hokkaido University, Sapporo 001-0021, Japan

\*Corresponding author. Tel: +66 430 09700 ext. 12371, Fax: +66 432 02373.

E-mail address: kingkaew@kku.ac.th (K.C. Chanapattharapol).

## Abstract

Titania (TiO<sub>2</sub>)-supported nickel (Ni) catalysts (3, 6, 12 and 20wt%; Ni/TiO<sub>2</sub>) were prepared by a sol-gel method to be used as a catalyst for carbon-dioxide (CO<sub>2</sub>) methanation. The catalytic activity tests were conducted with a fixed-bed reactor in the temperature range of 100–550 °C. The results showed that the CO<sub>2</sub> conversion increased with increasing Ni content and 20wt% Ni/TiO<sub>2</sub> exhibited the highest CO<sub>2</sub> conversion and the methane (CH<sub>4</sub>) yield which corresponded to the lowest apparent activation energy. Moreover, 20wt% Ni/TiO<sub>2</sub> also showed high stability under the CO<sub>2</sub> methanation stream for 72 h. The addition of Ni into TiO<sub>2</sub> during the sol-gel process modified the catalyst properties which affected to their catalytic activities, and the influence of Ni addition on the catalyst structure was studied by several techniques. The results on XRD and EXAFS revealed unit cell expansion and lattice distortion which indicated that nickel(II) cation was incorporated into TiO<sub>2</sub> lattice. Upon increasing in Ni content, the nickel(II) oxide (NiO) phase was observed indicating the high crystallinity of NiO and suppression of TiO<sub>2</sub> crystal growth. These effects led to smaller crystalline size of TiO<sub>2</sub> and higher surface area of the catalysts. The oxidation states of nickel and titanium were analyzed to be +2 and +4, respectively for fresh catalysts. After pretreatment by hydrogen (H<sub>2</sub>), Ni(II) was converted to Ni(0) and this electronic state was still unchanged during the course of methanation while Ti(IV) was kept unaltered for fresh catalysts and those during the reaction. However, the distortion or defect around Ti(IV) ions in Ni-loaded TiO<sub>2</sub> was observed as increase in Ti K-edge XANES pre-edge peaks. The addition of Ni led to formation of oxygen vacancy in TiO<sub>2</sub> lattice and NiO-phase formation which might act as the sites for CO<sub>2</sub>

35 and H<sub>2</sub> adsorption, respectively. Therefore, higher amount of adsorbed CO<sub>2</sub> and H<sub>2</sub> could  
36 enhance the surface reaction and also speed up the CO<sub>2</sub>-methanation.

37 **Keywords:** carbon-dioxide methanation; titania-supported nickel; XANES; EXAFS

38

## 39 1. Introduction

40 Recently, global warming is the most concerned problem of the world. The main reason  
41 for this problem is releasing high level of greenhouse gases (GHG) into the atmosphere.  
42 Carbon dioxide (CO<sub>2</sub>) has a large proportion of GHG. Enormous CO<sub>2</sub> emission level is a  
43 mainly result from human activities such as burning fossil fuel (coal, natural gas, and oil),  
44 transportation, deforestation, agriculture, electricity and industrial sectors. Therefore, reduction  
45 and utilization of CO<sub>2</sub> to produce value-added raw materials for chemical reactions are  
46 interested. CO<sub>2</sub> methanation is one of a powerful approach to utilize the CO<sub>2</sub> as a feedstock for  
47 producing CH<sub>4</sub>. This reaction is called the Sabatier reaction which is defined as the following  
48 equation;



50 The characteristic of this reaction are as follows; i) this reaction is a highly exothermic process,  
51 thus, CH<sub>4</sub> formation prefers to occur at low temperature and high pressure [1,2] ii) there is a  
52 kinetic barrier with eight-electron reduction process of the CO<sub>2</sub> (4+) to form CH<sub>4</sub> (4-) iii) CO<sub>2</sub>  
53 molecule is a strong linear structure with two double bond, so high dissociation energy must  
54 be consumed and iv) side reaction, reverse water gas shift (CO<sub>2</sub> + 4H<sub>2</sub>  $\rightleftharpoons$  CO + 2H<sub>2</sub>O) [3],  
55 occurs usually at high temperature which can produce an undesired product (CO). Therefore,  
56 from these limitations of this reaction, to increase the rate at low temperature, the catalyst must  
57 be employed.

58 Normally, the catalyst is consisted of two components; support and active component.  
59 The typical support properties are chemical stability, high thermal resistance and high surface  
60 area and porosity. The last properties have a significant role in catalytic reaction, since the  
61 adsorption and surface reaction processes are occurred on catalyst surface. An active  
62 component is another important component which is usually added onto the support with a  
63 small amount when compared with support. The function of an active site is selectively toward  
64 on adsorption of reactants, thus, an appropriate selectively active component is used for  
65 enhancing the adsorption and also speed-up the surface reaction. Consequently, tuning and  
66 modifying these two components properties can control and dominate the catalytic  
67 performance of the catalyst. For CO<sub>2</sub> methanation, enhancing the adsorption ability of two

68 reactants ( $\text{CO}_2$  and  $\text{H}_2$ ) on catalyst surface can possibly improve the surface reaction between  
69 these two adsorbed species and then the product formation rate also increases. Therefore,  
70 modifying catalyst with appropriate active site for  $\text{CO}_2$  and  $\text{H}_2$  adsorption can enhance the  
71 reaction rate. It is well known that  $\text{H}_2$  favors to adsorb on metal, especially transition metal  
72 group, various active metals are widely used for this reaction such as Rh, Ru, Pt and Pd [4-7].  
73 However, using the noble metals are limited due to their high cost and scarcity [8]. From this  
74 reason, nickel is more attractive to be used for  $\text{CO}_2$  methanation due to its relatively low price  
75 and also give high activity [9-11]. In order to enhance the  $\text{H}_2$  adsorption capacity, high  
76 dispersion of active metal on catalyst surface must be done. However, Ni can be deactivated  
77 by using at high temperature due to sintering process, thus, modifying the catalyst with  
78 resistance of this effect is also of interested. For  $\text{CO}_2$  adsorption, providing the basic sites on  
79 catalyst surface can improve the  $\text{CO}_2$  uptake via acid-base interaction. For this aspect, addition  
80 of basic metal oxide such as  $\text{La}_2\text{O}_3$ ,  $\text{CeO}_2$  and  $\text{MgO}$  is usually employed. Other method to  
81 increase  $\text{CO}_2$  uptake is to produce an oxygen vacancy which is reported as an adsorption site  
82 for  $\text{CO}_2$  molecule [12,13]. Oxygen vacancy can be formed within the metal oxide support by  
83 substitution of the host metal by adding metal with lower oxidation state than that of host metal  
84 [14,15]. Formation of oxygen vacancy by this way is usually used with a reducible support  
85 ( $\text{TiO}_2$ ,  $\text{CeO}_2$ ,  $\text{ZrO}_2$ , etc.), since the oxygen vacancy can mobile inside the lattice and plays an  
86 important role in redox process. Finally, it is seen that tuning and modifying of catalyst  
87 properties by considering the characteristic of reaction can produce the catalyst with great  
88 catalytic performance. It is reported that the synthesis method is strongly determined the  
89 physical and chemical properties of catalyst [11,16]. Many synthesis methods were reported to  
90 be used and provided a great catalytic performance [6,17,18]. However, the simple,  
91 environment friendly and inexpensive processes were usually preferred. The sol-gel method is  
92 one of the simplest and the most widely used due to its low cost of the required instrument,  
93 mild synthesis condition and also providing high homogeneous of the catalyst.

94 In this work, Ni was selected to be used as an active metal and  $\text{TiO}_2$  was a support.  
95 Since using  $\text{TiO}_2$  as a catalyst support for  $\text{CO}_2$  methanation is still developed, thus it is  
96 challenging to modify  $\text{TiO}_2$  catalysts which provide the excellent activity and produce the  
97 desired products for this reaction. Sol-gel method was used as a synthesis method to produce  
98 Ni/ $\text{TiO}_2$  catalysts with different Ni loading. The structural and surface properties of synthesized  
99 samples upon addition of Ni was investigated by X-ray diffraction (XRD),  $\text{N}_2$  adsorption-  
100 desorption, transmission electron microscopy (TEM),  $\text{H}_2$  temperature-programmed reduction  
101 (TPR),  $\text{H}_2$  chemisorption and thermogravimetric analysis. All strategies were used for studying

102 the effect of Ni addition for CO<sub>2</sub> methanation. Advanced analysis of local structures and  
103 oxidation states of probe metals (Ni and Ti) was determined by using X-ray absorption  
104 spectroscopy (XAS) which was including with X-ray absorption near-edge structure (XANES)  
105 and extended X-ray-absorption fine structure (EXAFS). The effect of Ni addition to enhance  
106 the CO<sub>2</sub> methanation was discussed based on the all characterized results.

107

## 108 **2. Experimental**

### 109 **2.1 Syntheses of TiO<sub>2</sub> and Ni-loaded TiO<sub>2</sub> catalysts**

110 All synthesized samples were prepared by sol-gel method using titanium(IV)  
111 isopropoxide (98%, Acros Organics) as a precursor. For pure TiO<sub>2</sub>, Ti precursor was mixed  
112 with glacial acetic acid (RCI Labscan) and 2-propanol (Carlo Erba Reagents) and then stirred  
113 for 30 min. The mixture was dropped wise with deionized water (DI) and vigorously stirred for  
114 starting hydrolysis reaction. Finally, the solution was dried in an oven at 110°C for 24 h and  
115 calcined at 500°C for 2 h to obtain bare TiO<sub>2</sub>.

116 In preparation of Nickel (Ni) modified TiO<sub>2</sub> catalysts, the titanium(IV)  
117 isopropoxide, glacial acetic acid and 2-propanol were mixed with the same manners as the  
118 above-mentioned pure-TiO<sub>2</sub> preparation. The desired amount of nickel nitrate (Carlo Erba  
119 Reagents) was dissolved with DI water and then dropped wise in the Ti precursor mixture. The  
120 solution was dried and calcined at the same conditions as pure TiO<sub>2</sub>. The synthesized samples  
121 were denoted as Xwt% Ni/TiO<sub>2</sub> where X = 3, 6, 12 and 20wt%.

### 122 **2.2 Characterization**

123 The structural properties of synthesized samples were characterized by X-ray  
124 diffraction (XRD) using Rigaku SmartLab X-ray diffractometer using Cu K<sub>α</sub> ( $\lambda = 0.154$  nm).  
125 The XRD pattern was collected in the  $2\theta$  range of 10° to 80°. Bragg's equation was used to  
126 determine the unit cell parameters of samples by using (101) crystallographic plane of anatase  
127 TiO<sub>2</sub>. The means of crystallite sizes of TiO<sub>2</sub> and Ni-loaded TiO<sub>2</sub> were calculated by the  
128 Scherer's equation:

$$129 \quad D = \frac{K\lambda}{\beta \cos\theta} \quad (2)$$

130 where  $D$  is the crystallite size,  $K$  is the shape factor,  $\lambda$  is the X-ray wavelength,  $\beta$  is the  
131 broadening at half maximum and  $\theta$  is the diffraction angle. In order to determine the strain  
132 induced by addition of Ni, the Williamson-Hall (W-H) plot method was used which can be  
133 expressed by the following equation;

134 
$$\beta \cos \theta = \frac{K\lambda}{D} + 4\varepsilon \sin \theta \quad (3)$$

135 where  $\varepsilon$  is the strain induced from crystal imperfection and distortion. The W-H plot shows a  
136 relationship between  $\beta \cos \theta$  and  $4\sin \theta$ . The strain ( $\varepsilon$ ) can be estimated from the slope of linear fit and  
137 the crystallite size ( $D$ ) can also be determined from y-intercept.

138 Nitrogen ( $N_2$ ) adsorption-desorption isotherms were recorded using a  
139 Quantachrome (previously Yuasa Ionics; Autosorb 6AG) surface-area and pore-size analyzer.  
140 Prior  $N_2$  adsorption, the sample was degassed at 200 °C for 2 h to remove the moisture on  
141 surface sample. Specific surface area, average pore size and pore volume were calculated by  
142 Brunnauer-Emmett-Teller (BET) equation. The specific surface area was commonly  
143 determined at relative pressure ( $P/P_0$ ) range between 0.1 to 0.3. Barrett-Joyner-Halenda (BJH)  
144 method was used to calculate the pore size distribution. The pore volume was measured at the  
145 relative pressure closed to unity ( $P/P_0 \sim 1$ ).

146 Hydrogen ( $H_2$ ) temperature-programmed reduction (TPR) was investigated by a  
147 Belcat B apparatus. A 20-mg portion of sample was pretreated by flowing with helium (He)  
148 at 120 °C for 30 min to clean up the surface. After cooling down, the mixture gases of  $H_2$  and  
149 argon (Ar) were flowed over the sample while the temperature was rose up to 1000 °C with  
150 ramping rate of 10 K  $min^{-1}$ . Thermal conductivity detector (TCD) was used to collect the  
151 change of thermal conductivity of the gas stream.  $H_2$  consumption was plotted as a function  
152 of temperature.

153 Transmission electron microscopy were performed by TEM, a FEI Tecnai G2 20 S-  
154 TWIN), to analyze particles sizes and morphologies of samples. The catalyst particles were  
155 dispersed in ethanol by sonication before dropping on copper grids.

156 Inductively coupled plasma-optical emission spectroscopy (ICP-OES) analysis was  
157 employed to measure the Ni contents. The powder (0.025 g) of sample was digested by a  
158 mixture of concentrated  $H_2SO_4$  (6 mL) and 30%  $H_2O_2$  (2 mL). The calibration curve was in the  
159 range of 0-30 ppm. An Optima 100 DVICO-OES (PerkinElmer) instrument was used to  
160 analyze Ni contents in a sample solution. The plasma was generated by an RF power with  
161 1300W, and plasma flow rate was 15 L/min. Auxillary and neubilizer flow rate was 0.2 L/min  
162 and 0.8 L/min, respectively. Emission light signal was detected by a CCD-array detector.

### 163 **2.3 $H_2$ chemisorption and $CO_2$ uptake**

164  $H_2$  chemisorption experiment was used to investigate the metal active sites on the  
165 catalyst surface which play an important role in enhancing the reaction rate. The  $H_2$

166 chemisorbed amount of all-loaded samples (3, 6, 12 and 20wt% Ni/TiO<sub>2</sub>) was carried out by  
167 Quantachrome Autosorb-1-C instrument. 200 mg of catalyst was first pretreated by flowing  
168 with He at 120 °C (ramp rate 20 °C min<sup>-1</sup>) for 30 min. After pretreatment, H<sub>2</sub> (99.999%, Thai  
169 Industrial Gas) was flowed over the sample during rising the temperature up to 300 °C (ramp  
170 rate 20 °C min<sup>-1</sup>) and the temperature was kept constant at this point for 120 min. Next, the  
171 sample was cooled down to 40 °C under vacuum and then H<sub>2</sub> was sequentially added to the  
172 sample. The amount of H<sub>2</sub> chemisorption was obtained by extrapolating method of the graph  
173 between volume of H<sub>2</sub> uptake and pressure. The monolayer of H<sub>2</sub> uptake ( $N_m$ ; μmol g<sup>-1</sup>) can be  
174 calculated by the following equation;

$$175 \quad N_m = 44.61 V_m \quad (4)$$

176 where  $V_m$  is the volume of monolayer uptake which can be determined by extrapolating method.  
177 CO<sub>2</sub> adsorption capacity of sample can be also used to explain the role of catalyst to catalyze  
178 the reaction rate. The CO<sub>2</sub> uptake was monitored by thermalgravimetric analysis (TGA, Pyris  
179 Diamond, Perkin Elmer Instrument). Al<sub>2</sub>O<sub>3</sub> was used as a reference. First, the synthesized  
180 sample was separately weighted and put on the aluminum pan and then placed on the sample  
181 holder. The maximum different weight between sample and reference was 0.5 mg. The sample  
182 was first pretreated by heating at 150 °C (10 °C min<sup>-1</sup>) for 45 min under N<sub>2</sub> flowing to remove  
183 an impurities. After that, CO<sub>2</sub> uptake was started by cooling down the sample to 40 °C under  
184 CO<sub>2</sub> flowing (100 mL min<sup>-1</sup>) for 60 min. Upon decreasing the temperature, the weight of sample  
185 was increased due to adsorption of CO<sub>2</sub> on solid surface. The CO<sub>2</sub> uptake can be calculated by  
186 differentiate the weight before and after adsorption.

#### 187 **2.4 CO<sub>2</sub> methanation catalytic activity test**

188 The CO<sub>2</sub> methanation-activity test was carried out in a fixed bed reactor with inner  
189 diameter of 0.6 mm. 50 mg of sample was placed at middle of pyrex reactor tube and  
190 sandwiched with quartz wool. Accurate temperature was monitored by K-type thermocouple  
191 which was located on the top of catalyst bed. The flow rates of the reactant gases were precisely  
192 controlled by mass flow controllers. Prior activity test, the synthesized catalyst was reduced  
193 under H<sub>2</sub> flow (50 mL min<sup>-1</sup>) at 450°C and maintained for 90 min. After that, the system was  
194 cooled down to 150°C to start the reaction. H<sub>2</sub> and CO<sub>2</sub> was used as a feed gas with a ratio of  
195 H<sub>2</sub>/CO<sub>2</sub> = 4 (balance with He). Total flow rate of feed gas was 40 mL min<sup>-1</sup> and GHSV was  
196 48,000 mL g<sup>-1</sup> min<sup>-1</sup>. The reaction temperatures were in the range of 100-550 °C. The effluent  
197 products and remaining reactants were analyzed by an online gas chromatography (Agilent

198 6890N Series, Agilent Technology) equipped with HEYSEP D Packed Column and TCD  
199 detector. Instrumental diagram of CO<sub>2</sub> methanation catalytic activity test set up is shown in  
200 Figure 1. CO<sub>2</sub> conversion, CH<sub>4</sub> and CO selectivity and yield were calculated by the following  
201 equations:

$$202 \quad X_{\text{CO}_2} = \left( \frac{F_{\text{CO}_2\text{in}} - F_{\text{CO}_2\text{out}}}{F_{\text{CO}_2\text{in}}} \right) \times 100 \quad (5)$$

$$203 \quad S_{\text{CH}_4, \text{CO}} = \left( \frac{F_{\text{CH}_4\text{out}} + F_{\text{COout}}}{F_{\text{CH}_4\text{out}} + F_{\text{COout}}} \right) \times 100 \quad (6)$$

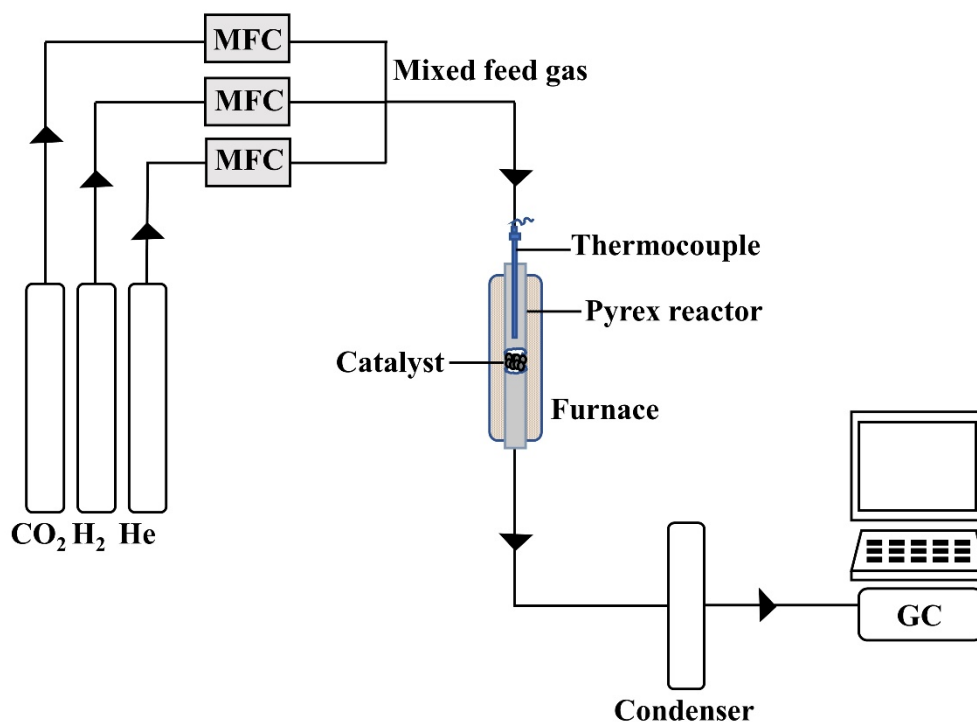
$$204 \quad Y_{\text{CH}_4, \text{CO}} = \left( \frac{X_{\text{CO}_2} \times S_{\text{CH}_4, \text{CO}}}{100} \right) \quad (7)$$

205 where,  $X_{\text{CO}_2}$  is the CO<sub>2</sub> conversion,  $S$  is the selectivity and  $Y$  is the yield.  $F$  is the molar flow  
206 rate of gas (mol s<sup>-1</sup>).

207 The rate of CO<sub>2</sub> methanation were measured in the temperature range of 240-290 °C  
208 to keep below 10% of CO<sub>2</sub> conversion. The rate of reaction was calculated using the following  
209 equation [19];

$$210 \quad \text{Rate} = \left( \frac{F_{\text{CO}_2}}{W} \right) \times X_{\text{CO}_2} \quad (8)$$

211 where,  $F_{\text{CO}_2}$  is the flow rate of CO<sub>2</sub> (mol s<sup>-1</sup>),  $W$  represents the weight of catalyst (g).



212 **Figure 1** Instrumental diagram of CO<sub>2</sub> methanation catalytic activity test.

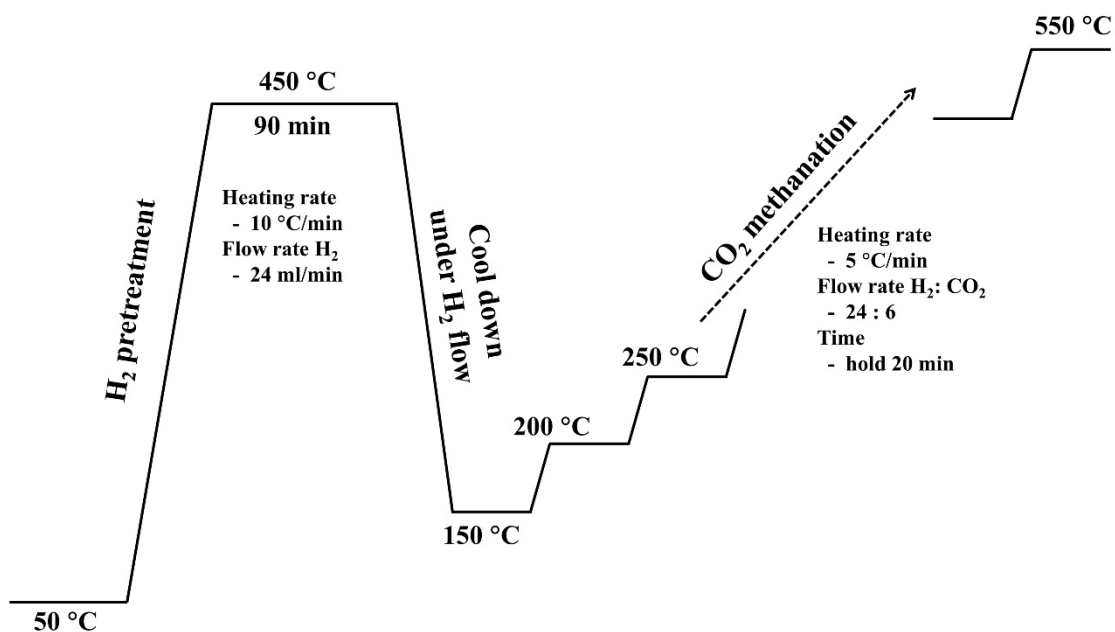
213

## 214 **2.5 X-ray Absorption Spectroscopy (XAS)**

### 215 **2.5.1 X-ray Absorption Near Edge Structure (XANES)**

216 X-ray Absorption Near Edge Structure (XANES) experiment was divided into  
 217 two parts; ex-situ and in-situ XANES experiments. The ex-situ XANES experiment was  
 218 conducted to investigate the oxidation state of Ni and Ti on the fresh catalysts. While in-situ  
 219 experiment was used to monitor the electronic state changing of Ni and Ti during CO<sub>2</sub>  
 220 methanation. The ex-situ XANES experiment was carried out on beamline 5.2 at Synchrotron  
 221 Light Research Institute (SLRI), Nakhon Ratchasima, Thailand [20,21]. The Ge (220) was used  
 222 as double crystal monochromator with energy resolution of  $2 \times 10^{-4}$  eV. The in-situ XANES  
 223 experiment was carried out on beamline 2.2 at Synchrotron Light Research Institute (SLRI),  
 224 Nakhon Ratchasima, Thailand. The Si (111) crystal was used as an Energy Dispersive  
 225 Monochromator (EDM) which covered photons energy of 2400-12000 eV. The linear image  
 226 sensor was a detector. Samples were prepared by mixing with Boron Nitride (BN) to a  
 227 homogeneous powder by using ball milling for 20 minutes. After that, the mixed solid sample

228 was compressed to a pellet. For ex-situ XANES experiment the pellet was placed on a Kapton  
229 tape which was stuck on the sample frame. The XANES spectra were collected in the K  
230 absorption edge energy for both Ni and Ti in transition mode. The ionization chamber was  
231 employed as a detector which was located in front of and behind the sample. For in-situ  
232 XANES experiment, the prepared sample in pellet form was placed in an in-situ cell. The in-  
233 situ XANES experiment condition was almost the same as CO<sub>2</sub> methanation catalytic activity  
234 test. The sample was pretreated with H<sub>2</sub> (24 mL min<sup>-1</sup>) during the temperature rose up from  
235 room temperature to 450 °C (heating rate of 5 °C min<sup>-1</sup>) and the XAS data were collected for  
236 each 10 °C increment. The reduction temperature (450 °C) was held for 1.5 h and the data was  
237 also recorded every 10 minutes. After pretreatment, the system was cooled down to 150 °C  
238 while the mixed feed gas between CO<sub>2</sub> (6 mL min<sup>-1</sup>) and H<sub>2</sub> (24 mL min<sup>-1</sup>) were purged through  
239 the sample to start the CO<sub>2</sub> methanation. At the starting state (150 °C), the reaction temperature  
240 was raised with the rate of 5 °C min<sup>-1</sup> to 200 °C and the data was recorded every 10 °C  
241 increment. Then, the temperature was kept constant at 200 °C for 20 minutes with recording of  
242 the data for every 10 minutes. The experiment was continuously conducted with the same  
243 procedure as above; i.e. the reaction temperature was also increased for each 50 °C with the  
244 heating rate of 5 °C min<sup>-1</sup> (recording data for each 10 °C increment) and held at that temperature  
245 for 20 minutes (recoding data for each 10 minutes). The reaction temperature of an in-situ  
246 experiment was in the range of 150-550 °C. Figure 2 shows the schematic of in-situ experiment  
247 for XANES.



248 **Figure 2** Schematic of in-situ experiment for XANES.

### 249 2.5.2 Extended X-ray Absorption Fine Structure (EXAFS)

250 Extended X-ray Absorption Fine Structure (EXAFS) was carried out to  
 251 determine the coordination number, interatomic distance and structural and thermal disorder  
 252 around Ni probe. The EXAFS was used to monitor the electronic state changing of Ni during  
 253 CO<sub>2</sub> methanation. The experiment was done on Beamline 5.2 at the Synchrotron Light  
 254 Research Institute (SLRI). (electron energy of 1.2 GeV; bending magnet; beam current 80-150  
 255 mA; 1.1 to 1.7 x 10<sup>11</sup> photon s<sup>-1</sup>). The Ni K-edge experiment was collected in transmission  
 256 mode (8333 eV). The X-ray incident and transmitted beam intensities were detected by  
 257 ionization chamber which was placed in front of and behind the sample. Samples were mixed  
 258 with Boron Nitride (BN) to form a homogeneous powder and compressed to a pellet. The  
 259 sample was pretreatment under H<sub>2</sub> flowing at 450 °C (20 mL min<sup>-1</sup>). The pretreatment  
 260 temperature was hold at this point for 90 min and the data were collected during this state.  
 261 Afterwards, the system was cooled down to 100 °C and CO<sub>2</sub> was purged at 5 mL min<sup>-1</sup> to start  
 262 the reaction. In each step, the reaction temperature was increased for each 50 °C and kept  
 263 constant for 30 min with collecting the EXAFS spectra. The experiment was continuously run  
 264 by increasing reaction temperature from 100 to 550 °C.

265 The fine structure of EXAFS region is expressed in terms;  $\chi(E) = \mu(E) -$   
 266  $\mu_0(E) / \Delta\mu_0(E)$ , where  $\mu(E)$  is the absorption coefficient,  $\mu_0(E)$  is the smooth background

267 function and  $\Delta\mu_0$  is the absorption edge. The wave behavior of photoelectron ( $k$ ) can be written  
 268 by X-ray energy as;  $k = \sqrt{2m_e(E-E_0)/h^2}$ , where  $E_0$  is the absorption edge energy and  $m_e$  is the  
 269 electron mass. The oscillation in  $\chi(k)$  model of EXAFS region is corresponding to

$$270 \quad \chi(k) = \sum_j \frac{N_j S_0^2 f_j(k) e^{-2R_j/\lambda} e^{-2k^2\sigma_j^2}}{kR_j^2} \sin[2kR_j + \delta_j(k)] \quad (9)$$

271 where  $N_j$  is the number of neighboring atoms,  $R_j$  is the neighboring distance and  $\sigma_j^2$  is the  
 272 disorder of neighboring distance.  $F(k)$  and  $\delta(k)$  are the scattering-amplitude and phase-shift.  
 273  $S_0^2$  is the amplitude reduction factor. The data is usually expressed by Fourier transformation  
 274 from  $\chi(k)$  to  $R$  space to study local structure around neighboring atom as

$$275 \quad \chi(R) = \frac{1}{\sqrt{2\pi}} \int_{k_{\min}}^{k_{\max}} k^n \chi(k) W(k) e^{i2kR} dk \quad (10)$$

276 The next step is normalization of the experiment data by ATHENA program. The  
 277 spectra were amplified by  $k^2$  weight with window in  $R$  space range of 1-5 Å and  $k$  range of 3-  
 278 10 Å<sup>-1</sup>. To determine the local structure of Ni-loaded TiO<sub>2</sub> in CO<sub>2</sub> methanation, Ni foil was  
 279 used as a model fitting of EXAFS data. The experimental EXAFS data was fitted by ARTEMIS  
 280 program.

281

### 282 3. Results and discussion

#### 283 3.1 Catalytic performances of CO<sub>2</sub> methanation

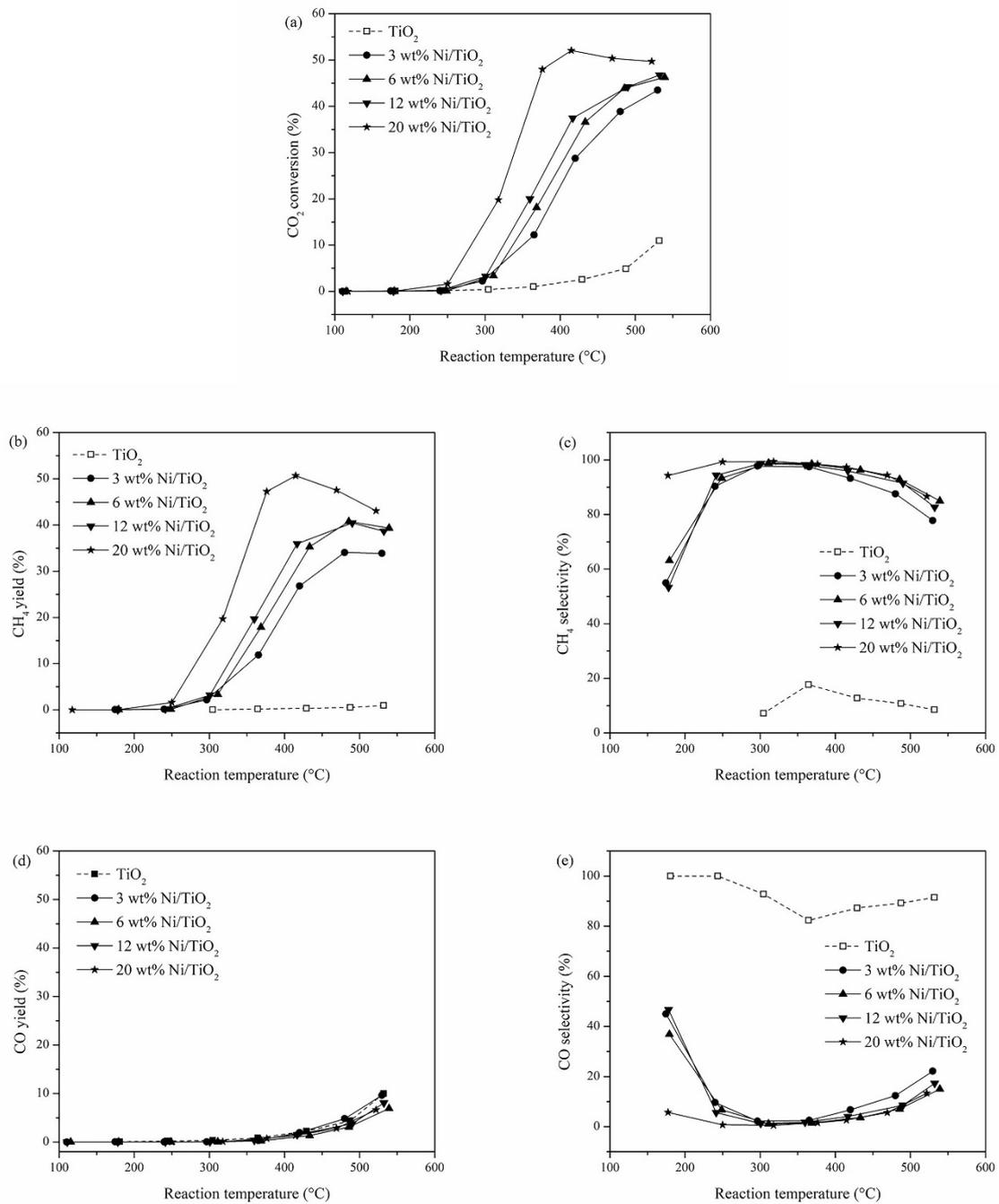
284 The CO<sub>2</sub> methanation was carried out at reaction temperature range of 100-550 °C  
 285 with a weight hourly space velocity (WHSV) of 48,000 mL g<sup>-1</sup> h<sup>-1</sup>. Catalytic performances of  
 286 TiO<sub>2</sub>, 3, 6, 12 and 20wt% of Ni-loaded TiO<sub>2</sub> samples were displayed in term of CO<sub>2</sub> conversion  
 287 as a function of temperature. The CO<sub>2</sub> conversion, products (CH<sub>4</sub> and CO) selectivities and  
 288 yields are represented in Figure 3(a)-3(e). The CO<sub>2</sub> conversion for all samples increased  
 289 according to reaction temperature. However, upon the addition of Ni onto TiO<sub>2</sub>, shifting of CO<sub>2</sub>  
 290 conversion toward lower reaction temperature were observed. For bare TiO<sub>2</sub>, the catalytic  
 291 performance was almost inactive with illustrating of the lowest CO<sub>2</sub> conversion and low CH<sub>4</sub>  
 292 yield and selectivity, while CO selectivity was relatively high. In contrast, Ni supported TiO<sub>2</sub>  
 293 catalysts (3, 6, 12 and 20wt% Ni/TiO<sub>2</sub>) exhibited a dramatically enhance in catalytic activities  
 294 which can be observed by increasing of CO<sub>2</sub> conversion at lower reaction temperature. Upon  
 295 addition of Ni, product selectivities were changed, i.e., CH<sub>4</sub> yield were developed and  
 296 selectivity toward CH<sub>4</sub> were almost 100%, while CO yield and selectivity were rapidly dropped  
 297 to lower 10%. This result indicated that addition of Ni onto TiO<sub>2</sub> support improved the desired

298 product (CH<sub>4</sub>) selectivity and suppressed an unwanted product (CO). Increase of Ni  
299 concentration resulted in increasing of CO<sub>2</sub> conversion and CH<sub>4</sub> yield, while CH<sub>4</sub> selectivities  
300 were almost nearly the same (~100%) for all samples. However, 20wt% Ni/TiO<sub>2</sub> exhibited the  
301 highest CO<sub>2</sub> conversion and CH<sub>4</sub> yield, it is noteworthy that the CH<sub>4</sub> selectivity was almost  
302 100% in the wide range of reaction temperature (150-450 °C).

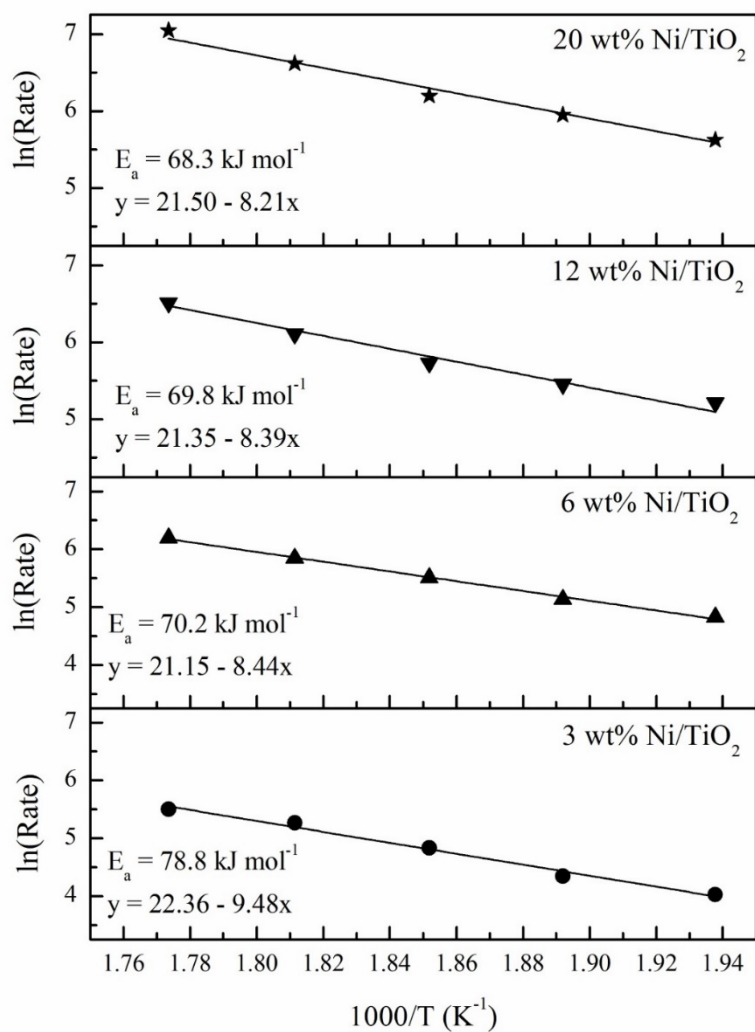
303 In order to study the kinetic parameter (apparent activation energy), heat and mass  
304 transfer effects were checked during measurement of reaction rate by the Koros-Nowak test  
305 [22]. The catalytic performances were tested by using samples with different of Ni active site  
306 loading (6wt% and 20wt% Ni) at 250 °C at feed gas ratio of H<sub>2</sub>/CO<sub>2</sub>/He = 24:6:10 and WHSV  
307 = 48,000 mL g<sup>-1</sup> h<sup>-1</sup>. The results revealed that the CO<sub>2</sub> conversion of 6wt% Ni/TiO<sub>2</sub> and 20wt%  
308 Ni/TiO<sub>2</sub> were 1.90 and 4.30 %, respectively, while turn over frequency (TOF) were almost the  
309 same values (0.27 s<sup>-1</sup> and 0.25 s<sup>-1</sup>, respectively). Therefore, it was attributed that heat and mass  
310 transfer were absence for this experiment condition.

311 The apparent activation energy (E<sub>a</sub>) was usually used to elucidate the catalytic  
312 performance in enhancing the reaction rate. This value can be obtained by using the Arrhenius  
313 equation ( $k = Ae^{-E_a/RT}$ ). The plotting between ln(rate) and reciprocal of absolute temperature  
314 (1/T) was constructed. The slope of the linear graph was used to calculate the apparent  
315 activation energy. Figure 4 illustrates the Arrhenius plots of 3, 6, 12 and 20wt% Ni/TiO<sub>2</sub>. It  
316 was seen that the apparent activation energies were decreased with increasing of Ni content (E<sub>a</sub>  
317 ranges between 68-78 kJ mol<sup>-1</sup>). Reduction of apparent activation energy upon more Ni  
318 addition indicated that lower kinetic barrier for catalyzing toward the reaction, thus, the  
319 catalytic activity can be enhanced. The E<sub>a</sub> values were corresponded to the catalytic activities  
320 results that 20wt% Ni/TiO<sub>2</sub> exhibited the highest CO<sub>2</sub> conversion due to the lowest E<sub>a</sub> for this  
321 reaction. The long-term stability test is also an important property to determine the efficiency  
322 of catalyst in thermal sintering for industrial scale. Figure 5 exhibits the CO<sub>2</sub> conversion and  
323 CH<sub>4</sub> yield of 20wt% Ni/TiO<sub>2</sub> in CO<sub>2</sub> methanation for 72 h. The stability test of 20wt% Ni/TiO<sub>2</sub>  
324 was done by keeping the reaction temperature at 420 °C since this temperature exhibited the  
325 highest in CO<sub>2</sub> conversion. The CO<sub>2</sub> conversion was stable during 72 h on stream (decrease

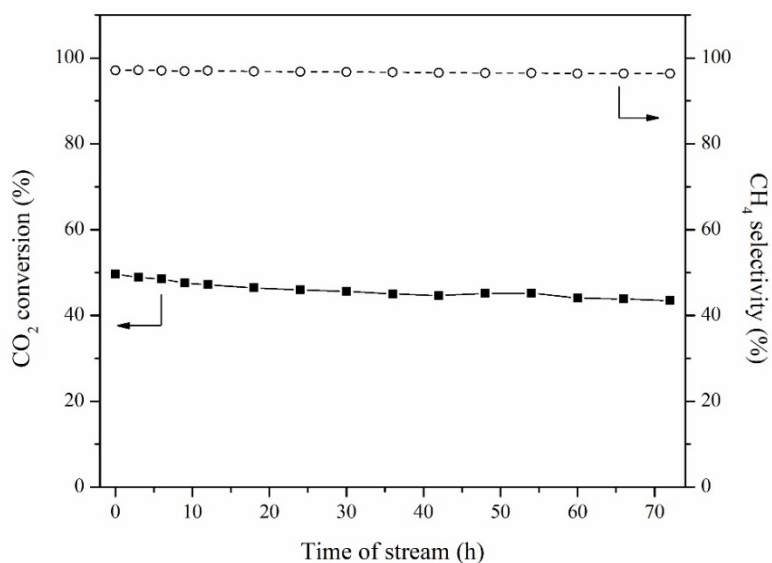
326 not over 10%) which was corresponded to consistency of CH<sub>4</sub> selectivity (almost 100%) for  
 327 this sample.



328 **Figure 3** (a) CO<sub>2</sub> conversion, (b) CH<sub>4</sub> yield, (c) CH<sub>4</sub> selectivity, (d) CO yield and (e) CO  
 329 selectivity of all catalysts; TiO<sub>2</sub>, 3, 6, 12 and 20wt% Ni-loaded TiO<sub>2</sub> by using  
 330 H<sub>2</sub>/CO<sub>2</sub>/He = 24:6:10, total flow rate 40 mL min<sup>-1</sup>, WHSV = 48,000 mL g<sup>-1</sup> h<sup>-1</sup> at  
 331 reaction temperature 100-550 °C.



332 **Figure 4** Arrhenius plots for the CO<sub>2</sub> methanation with different Ni contents on TiO<sub>2</sub>; TiO<sub>2</sub>,  
 333 3, 6, 12 and 20wt% Ni/ TiO<sub>2</sub>.



334 **Figure 5** CO<sub>2</sub> conversion and CH<sub>4</sub> selectivity over 20wt% Ni/ TiO<sub>2</sub> during long-term stability  
 335 test at reaction temperature of 420 °C, H<sub>2</sub>/CO<sub>2</sub>/He = 24:6:10 and WHSV = 48,000  
 336 mL g<sup>-1</sup> h<sup>-1</sup>.

### 337 3.2 Standard characterization

#### 338 3.2.1 X-ray diffraction (XRD)

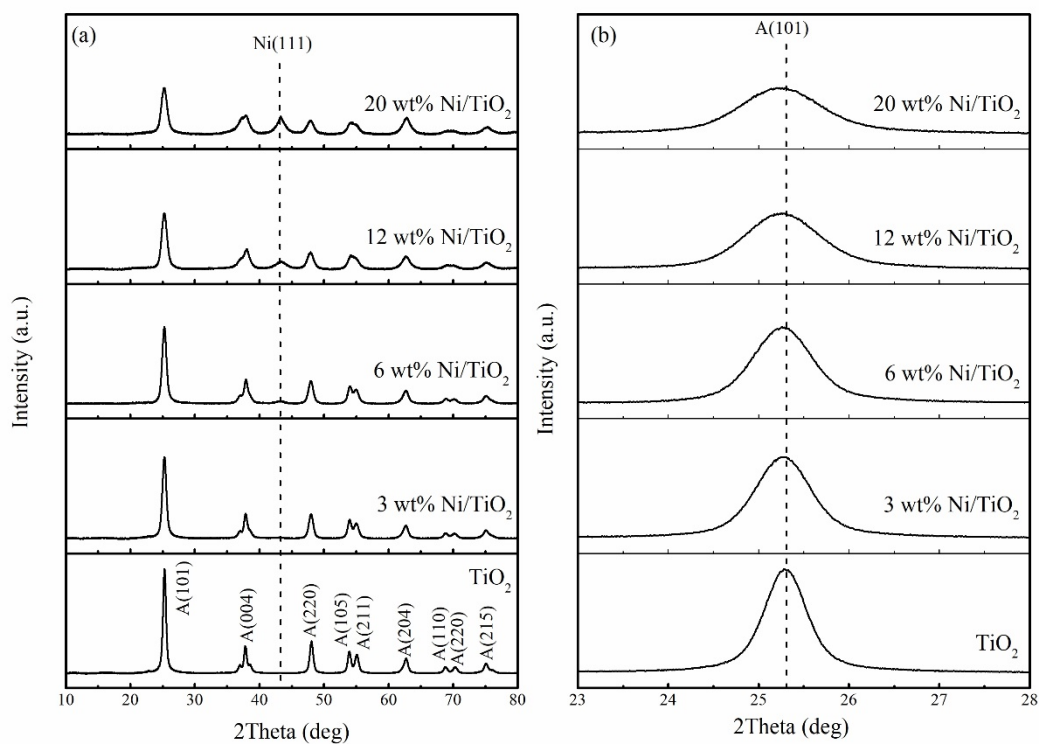
339 XRD patterns of TiO<sub>2</sub> with various Ni contents (3, 6, 12 and 20wt%) are  
 340 shown in Figure 6. The XRD peaks of TiO<sub>2</sub> were observed at 25.3°, 37.8°, 48.0°, 53.9°, 55.1,  
 341 62.7, 68.9°, 70.3° and 75.1° which were corresponding to (101), (004), (200), (105), (211),  
 342 (204), (110), (220) and (215) planes of anatase structure with using JICST database (from The  
 343 Crystallographic Society of Japan). For all Ni-loaded catalysts (3, 6, 12 and 20wt%), the  
 344 anatase structure of TiO<sub>2</sub> remained unchanged. However, the intense diffraction peaks  
 345 decreased when increasing of Ni loading. The lowering of these peaks related to reducing of  
 346 crystallinities and crystalline sizes of TiO<sub>2</sub>. This indicated that addition of Ni into TiO<sub>2</sub> during  
 347 sol-gel process can prevent the crystalline growth of TiO<sub>2</sub> [23]. It was found that the crystalline  
 348 sizes of TiO<sub>2</sub> were reduced with more added of Ni content as illustrated in Table 1. In addition,  
 349 shifting of diffraction peaks to lower diffraction angles were also observed which indicated to  
 350 unit cell expansion. This phenomenon resulted from the substitution of Ti<sup>4+</sup> ion by larger Ni<sup>2+</sup>  
 351 ion (ionic radii of Ni<sup>2+</sup> = 0.72 Å and Ti<sup>4+</sup> = 0.68 Å for 6-fold coordination). The unit cell of  
 352 TiO<sub>2</sub> catalyst was enlarged upon increase of Ni content which indicated to more incorporation  
 353 of Ni<sup>2+</sup> ions into TiO<sub>2</sub> lattice [24-26]. To confirm the incorporation of adding metal into host  
 354 lattice, the Williamson-Hall (W-H) parameter was used. Upon incorporation of adding metal,

355 the host lattice was distorted and strain was increased. In this case,  $\text{Ti}^{4+}$  site was replaced by  
356  $\text{Ni}^{2+}$  divalent cation, thus oxygen vacancies were expected to form. Therefore, the W-H  
357 parameter can indicate to the degree of incorporation of adding metal [27,28]. Table 1  
358 summarizes the unit cell parameter, unit cell volume and lattice strain of all synthesized  
359 samples. It can be seen that the unit cell parameter and unit cell volume were increased with  
360 increasing of Ni loading. The lattice strain was also enlarged which indicated to higher amount  
361 of incorporated  $\text{Ni}^{2+}$  into  $\text{TiO}_2$  lattice upon increase of Ni content.

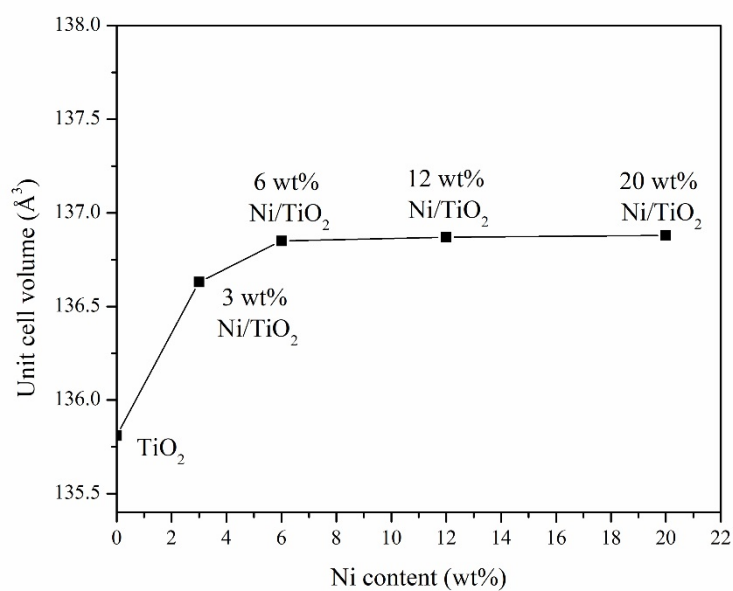
362 Besides the  $\text{TiO}_2$  anatase diffraction peaks, another additional important peak was also  
363 observed, i.e., NiO diffraction peak at  $43.5^\circ$ . This peak was attributed to a face centered-cubic  
364 crystalline structure of NiO. It was noteworthy that this peak was not observed in the low Ni  
365 content sample (3wt% Ni/ $\text{TiO}_2$ ). This was probably due to completely incorporate of adding  
366 Ni ion into  $\text{TiO}_2$  and the solid solution was formed. In contrast, the NiO diffraction peak was  
367 obviously appeared for Ni loading  $\geq 6\text{wt}\%$ . This result can imply that addition of Ni was  
368 existed in two forms, i.e., incorporation of Ni ion into  $\text{TiO}_2$  lattice and dispersion of NiO onto  
369  $\text{TiO}_2$  surface. Therefore, there was a limitation or saturated level of incorporation of Ni ion into  
370  $\text{TiO}_2$  lattice and then the excess of Ni added amount can disperse onto  $\text{TiO}_2$  surface. From this  
371 behavior, both shifting of XRD peaks and existing of NiO peak were observed. In order to  
372 estimate the saturated value of Ni concentration, the relationship between unit cell volume and  
373 Ni content was constructed as illustrated in Figure 7. It can be seen that the unit cell volume  
374 was increased upon addition of Ni and the expansion of lattice was almost constant at higher  
375 Ni loading more than 6wt%. Form this plot, the saturated Ni incorporated amount was in the  
376 range between 3-6wt%. Therefore, from our results, we assumed that the saturated Ni  
377 incorporated amount was 3wt% which mean that all Ni addition was incorporated into  $\text{TiO}_2$   
378 lattice at this added level. Increasing of Ni content at higher amount than 6wt%, the excess  
379 amount of adding Ni was dispersed onto  $\text{TiO}_2$  surface and more intense of NiO diffraction peak  
380 was observed which indicated to higher crystallinity and crystalline size of NiO phase. To  
381 evidence the substitution of Ni ion into  $\text{TiO}_2$  lattice and dispersion of NiO phase onto catalyst  
382 surface, X-ray Absorption Spectroscopy (XAS) results were used and discussed in the next  
383 part.

384

385



386 **Figure 6** (a) XRD diffraction patterns of all catalysts.  
 387 (b) magnification of (101) crystallographic plane for all catalysts to compare  
 388 the shifting of the diffraction peak.



389 **Figure 7** Relationship between unit cell parameters of all catalysts against Ni content.  
 390

391 **Table 1** Structural and physical properties of all synthesized samples including lattice  
 392 parameter, cell volume, crystal size, lattice strain and Ni content.

Samples	Lattice parameter <sup>a</sup> (Å)		Cell volume <sup>a</sup> (Å <sup>3</sup> )	Crystal size <sup>b</sup> (nm)		Lattice strain <sup>c</sup>	Ni contents <sup>d</sup> (wt%)
	a = b	c		Anatase	Ni		
TiO <sub>2</sub>	3.778	9.516	135.81	14.92	-	3.65 × 10 <sup>-4</sup>	-
3wt% Ni/TiO <sub>2</sub>	3.791	9.506	136.63	11.41	3.99	7.35 × 10 <sup>-4</sup>	2.92
6wt% Ni/TiO <sub>2</sub>	3.793	9.501	136.85	10.63	4.55	1.66 × 10 <sup>-3</sup>	6.07
12wt% Ni/TiO <sub>2</sub>	3.801	9.475	136.87	8.37	3.98	4.03 × 10 <sup>-3</sup>	13.5
20wt% Ni/TiO <sub>2</sub>	3.780	9.483	136.88	7.84	5.31	7.83 × 10 <sup>-3</sup>	21.5

<sup>a</sup>Calculated from the plane (101), (004), (100) by Bragg's equation.

<sup>b</sup>Calculated from the plane (101) for anatase and (111) for Ni using Scherer's equation.

<sup>c</sup>Calculated from Williamson-Hall (W-H).

<sup>d</sup>Calculated from ICP-OES results.

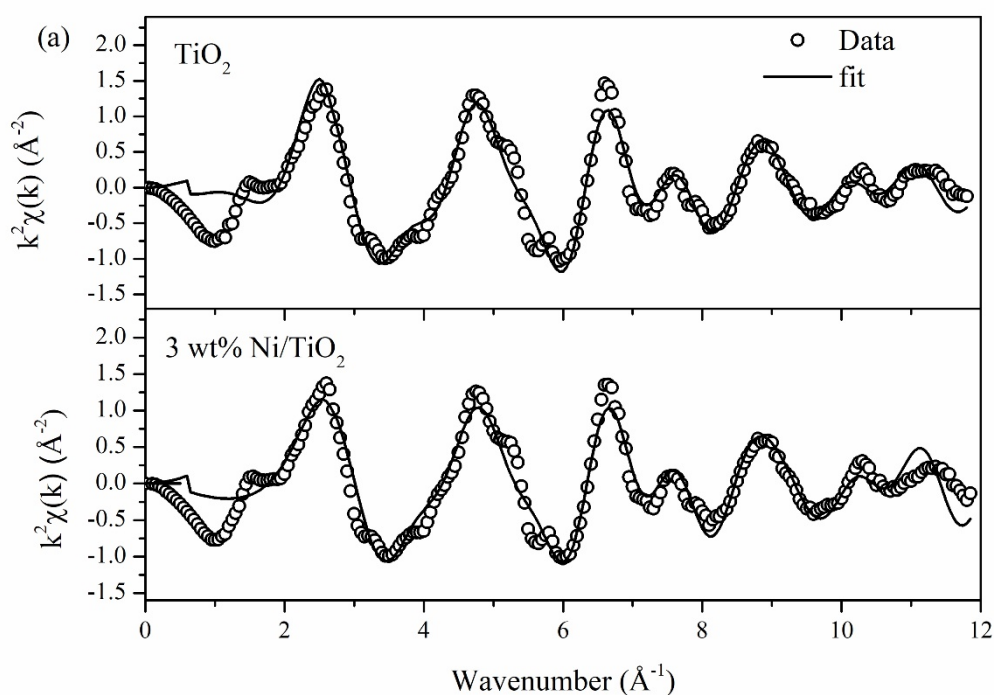
393 **3.2.2 Structural study of Ni-loaded TiO<sub>2</sub> catalysts by X-ray Absorption**  
 394 **Spectroscopy (XAS)**

395 As discussed above that there were two forms of Ni addition; Ni substitution  
 396 and NiO dispersion, thus in this part, X-ray Absorption Spectroscopy (XAS) results were used  
 397 to evidence the existing of these two forms. The first form, substituted of Ni ion into TiO<sub>2</sub>,  
 398 Extended X-ray Absorption Fine Structure (EXAFS) of 3wt% Ni/TiO<sub>2</sub> was analyzed and  
 399 discussed to confirm the substitution of Ni ion into TiO<sub>2</sub> lattice. Another form, dispersed NiO,  
 400 linear combination between substitution Ni and NiO was performed and then the percentage  
 401 composition of substitution Ni and NiO were determined.

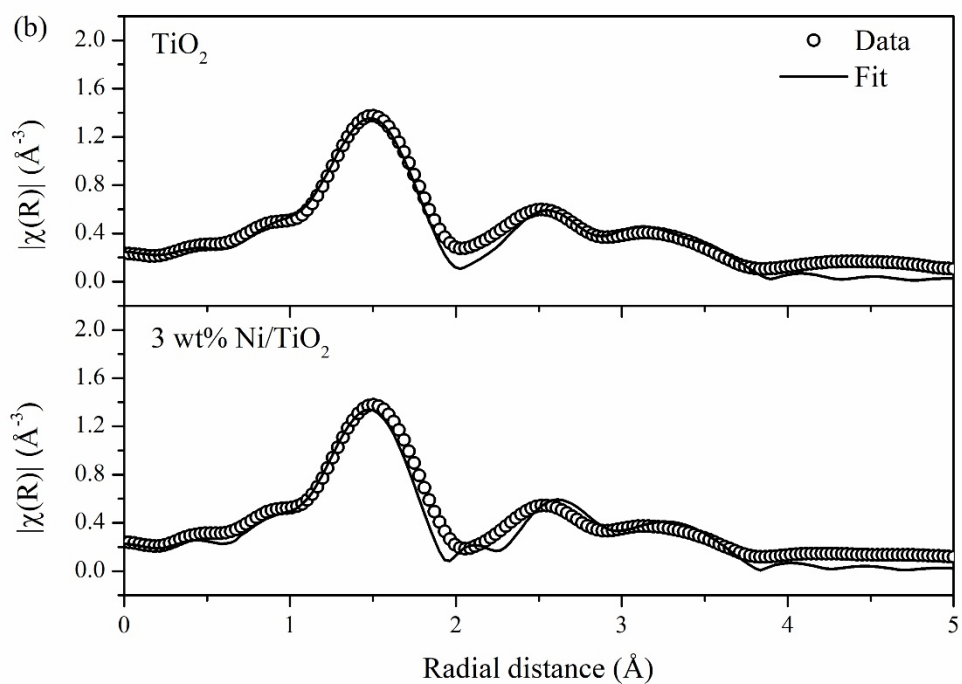
402 For Ni substitution form, analysis of EXAFS result of 3wt% Ni/TiO<sub>2</sub> was  
 403 used since we assumed the complete substitution of all added Ni amount for this sample. The  
 404 Ti K-edge EXAFS oscillation spectra and Fourier transformed functions for TiO<sub>2</sub> and 3wt%  
 405 Ni/TiO<sub>2</sub> by using anatase TiO<sub>2</sub> (space group I4<sub>1</sub>/amd) as a model for fitting are shown in Figure  
 406 8. For Ni-loaded TiO<sub>2</sub> sample, the FT-EXAFS spectra were obtained by fitting with anatase  
 407 TiO<sub>2</sub> and replacing one atom of the nearest Ti atom with Ni. The k<sup>2</sup>-weighted Fourier transform  
 408 was used (Figure 8(a)). The weight EXAFS data in k space was in the range from 3-10 Å<sup>-1</sup> and  
 409 was transformed to R space without phase collection (Figure 8(b)). The structural parameters  
 410 of TiO<sub>2</sub> and 3wt% Ni/TiO<sub>2</sub> for Ti K-edge are summarized in Table 2. For Figure 8(b), the sharp  
 411 peak of TiO<sub>2</sub> at ~1.5 Å was referred to the oscillation of Ti-O in the first shell. Upon

412 incorporation of Ni in second shell of TiO<sub>2</sub> lattice, the Ti–O bond distance were distorted (as  
413 shown in Table 2), while the Ti–Ni bond length was elongated due to substitution by larger  
414 cation and then resulted in shortening of Ti–Ti bond distance.

415 From the results of XRD, it can be seen that both Ni incorporated and  
416 dispersed phase of NiO were observed, especially for high Ni content than 6wt%. In order to  
417 determine the compositions of these two forms of Ni species, linear combination of XANES  
418 spectra were employed. For this approach, we assumed that all Ni loading at 3wt% was  
419 completely substituted into TiO<sub>2</sub> lattice, thus the excess amount of added Ni (higher than 3wt%)  
420 was existed in NiO dispersed form. Therefore, the linear combination between substituted Ni  
421 and dispersed NiO was constructed and was used as a standard to estimate the composition  
422 between two forms of Ni species. For this work, Ni K-edge XANES spectrum of 3wt% Ni/TiO<sub>2</sub>  
423 was used as a standard for Ni substitution while that of NiO was used as a standard for NiO  
424 dispersion phase. Figure 9 displays the percentage of two forms of Ni species obtained from  
425 linear combination fitting. It was seen that NiO phase increased with Ni content which was  
426 corresponding to XRD results.



427 **Figure 8** (a) Ti K-edge EXAFS oscillation data with  $k^2\chi(k)$  for TiO<sub>2</sub> and 3wt% Ni/TiO<sub>2</sub>.



428 **Figure 8** (b) Fourier transform data of Ti K-edge EXAFS for TiO<sub>2</sub> and 3wt% Ni/TiO<sub>2</sub>.

429 **Table 2** Structural parameter for Ti K-edge EXAFS fitting analysis.

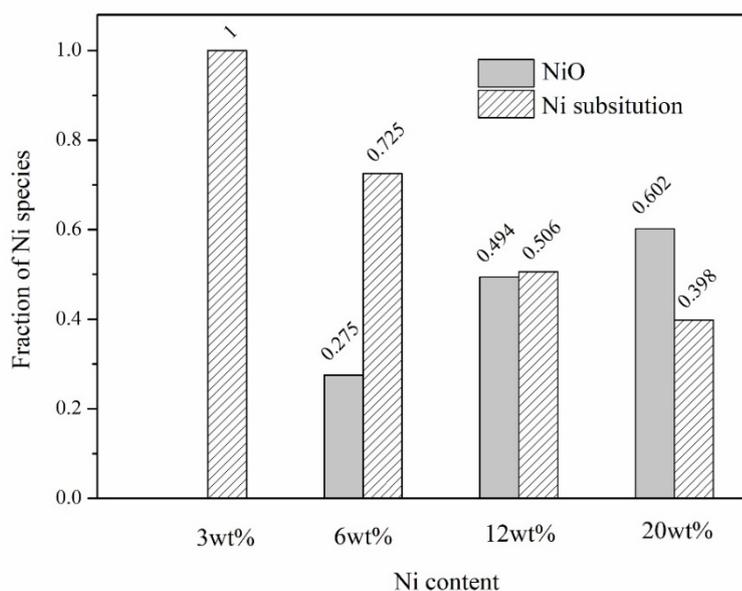
Samples	Shells	Best fit EXAFS parameters			
		N	$\sigma^2$	$\Delta E$ (eV)	R (Å)
TiO <sub>2</sub>	Ti-O	2.3	0.003	1.439	1.908
	Ti-O	1.2	0.001		1.996
	Ti-Ti	2.3	0.007		3.088
3wt% Ni/TiO <sub>2</sub>	Ti-O	1.9	0.001	1.474	1.927
	Ti-O	0.9	0.003		1.947
	Ti-Ti	1.4	0.002		3.051
	Ti-Ni	0.5	0.003		3.291

430

431

432

433



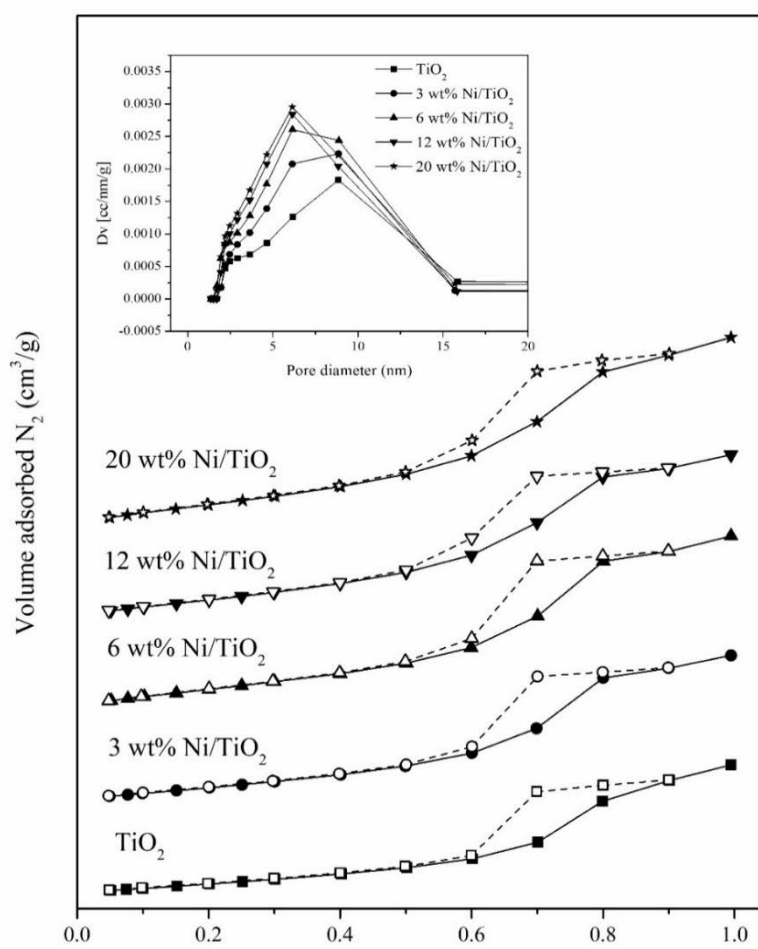
434 **Figure 9** The comparison between Ni substitution amount and NiO phase of all Ni-  
 435 loaded catalysts which obtained from comparing to a linear combination of XANES data of  
 436 Ni K-edge between 3wt% Ni/TiO<sub>2</sub> and NiO.

### 437 3.2.3 Surface and physical properties of catalysts

438 The surface properties of TiO<sub>2</sub> and modified-TiO<sub>2</sub> catalysts were estimated  
 439 by N<sub>2</sub> adsorption-desorption technique. The N<sub>2</sub> adsorption-desorption isotherms are displayed  
 440 in Figure 10. All isotherms exhibited an adsorption-desorption feature corresponded to  
 441 mesoporous materials. The surface area, pore size and pore volume of samples are summarized  
 442 in Table 3. The BET surface area of pure TiO<sub>2</sub> was 72 m<sup>2</sup>/g with pore volume of 0.15 cm<sup>3</sup>/g.  
 443 The Ni modified TiO<sub>2</sub> samples exhibited higher BET surface area and pore volume than that  
 444 of original TiO<sub>2</sub> upon increasing of Ni addition amount. The surface area of 3, 6, 12 and 20wt%  
 445 Ni/TiO<sub>2</sub> were ca. 92, 95, 100 and 108 m<sup>2</sup>/g, respectively. These results were in agreement with  
 446 XRD analysis which mentioned the prevention of anatase crystal growth by Ni addition and  
 447 led to lowering of TiO<sub>2</sub> crystalline sizes. Higher surface area was important to improve the  
 448 active surface sites to adsorb gas substrates for CO<sub>2</sub> methanation [29]. The pore size  
 449 distributions of the synthesized samples were in the range of 2-16 nm (inset). The pore diameter  
 450 distributions of TiO<sub>2</sub> and 3wt% Ni/TiO<sub>2</sub> gained the maximum value at 9 nm whereas higher Ni  
 451 contents samples (6, 12 and 20wt% Ni/TiO<sub>2</sub>) provided the smaller of diameter at a maximum  
 452 peak around 6 nm. Pore volumes of Ni-added samples were higher than that of pure TiO<sub>2</sub>.

453 The percentage of added Ni content in all Ni-loaded catalysts were  
 454 determined by inductively couple plasma-optical emission spectroscopy and the results are  
 455 summarized in Table 1. The obtained results of Ni content from ICP-OES in all Ni-loaded  
 456 catalysts exhibited a similar value to nominated added amount (2.92, 6.07, 13.5 and 21.5wt%  
 457 Ni for 3, 6, 12 and 20wt% Ni/TiO<sub>2</sub>, respectively).

458 The morphology of fresh TiO<sub>2</sub> and Ni supported TiO<sub>2</sub> are showed in Figure  
 459 11(a-e). The shape of particles for all samples were uniformly spherical and there was no  
 460 change of the anatase morphology for all Ni catalysts. The means of anatase particle sizes were  
 461 approximately in the range of 8-15 nm and the particle sizes were decreased upon increasing  
 462 of Ni content which was in agreement with XRD results. NiO was characterized using high-  
 463 resolution TEM for 20wt% Ni/TiO<sub>2</sub> resulting in Figure 11(f). The detection of lattice spacing  
 464 0.210 nm can be indexed as (200) plane of FCC Ni which were related to XRD patterns. This  
 465 result was confirmed the existence and dispersion of NiO.



484 **Figure 10** N<sub>2</sub> adsorption-desorption isotherms<sup>o</sup> and pore size distribution (inset) of all  
 485 catalysts; TiO<sub>2</sub>, 3, 6, 12 and 20wt% Ni-loaded TiO<sub>2</sub>. Solid symbol is adsorption  
 486 branch and open symbol is desorption branch.

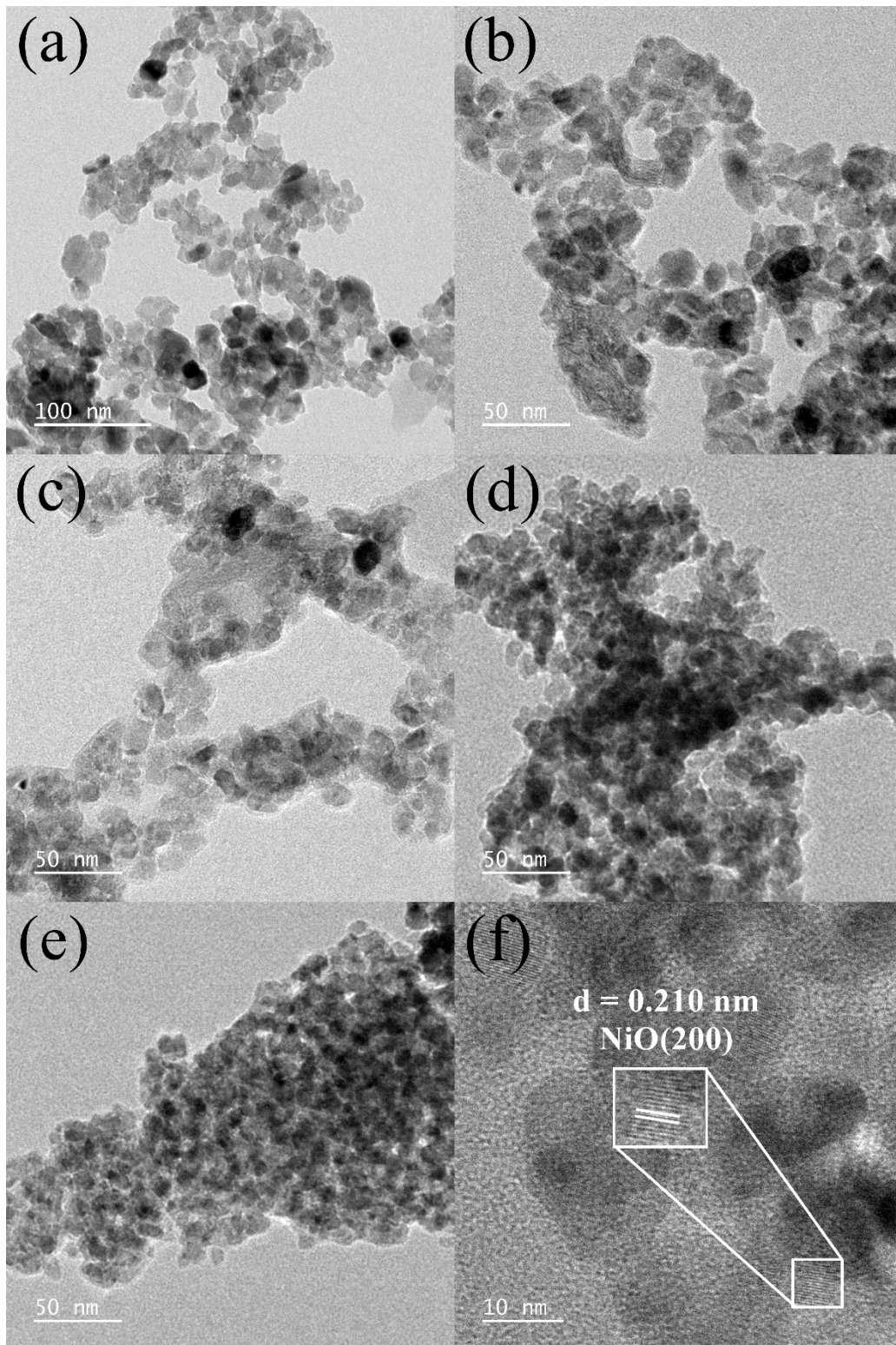
487 **Table 3** Surface properties of samples (TiO<sub>2</sub>, 3, 6, 12 and 20wt% Ni/TiO<sub>2</sub>).

Samples	Surface area <sup>a</sup> (m <sup>2</sup> /g)	Pore volume <sup>a</sup> (cm <sup>3</sup> /g)	Pore size <sup>a</sup> (nm)	H <sub>2</sub> consumption <sup>b</sup> (mmol/g)	H <sub>2</sub> chemisorbed <sup>c</sup> (μmol/g)
TiO <sub>2</sub>	71.48	0.1490	8.340	-	-
3wt% Ni/TiO <sub>2</sub>	91.80	0.1743	7.596	13.9	5.8
6wt% Ni/TiO <sub>2</sub>	95.41	0.1776	7.745	31.1	13.8
12wt% Ni/TiO <sub>2</sub>	100.3	0.1749	6.947	62.5	25.5
20wt% Ni/TiO <sub>2</sub>	107.6	0.1934	7.191	76.2	43.4

<sup>a</sup>Estimated from N<sub>2</sub> adsorption-desorption.

<sup>b</sup>Estimated from H<sub>2</sub>-TPR.

<sup>c</sup>Estimated from H<sub>2</sub> chemisorption.



488 **Figure 11** TEM images of (a) TiO<sub>2</sub>, (b) 3, (c) 6, (d) 12, (e) 20wt % Ni-loaded TiO<sub>2</sub> and  
489 (f) HRTEM for 20wt % Ni-loaded TiO<sub>2</sub>.

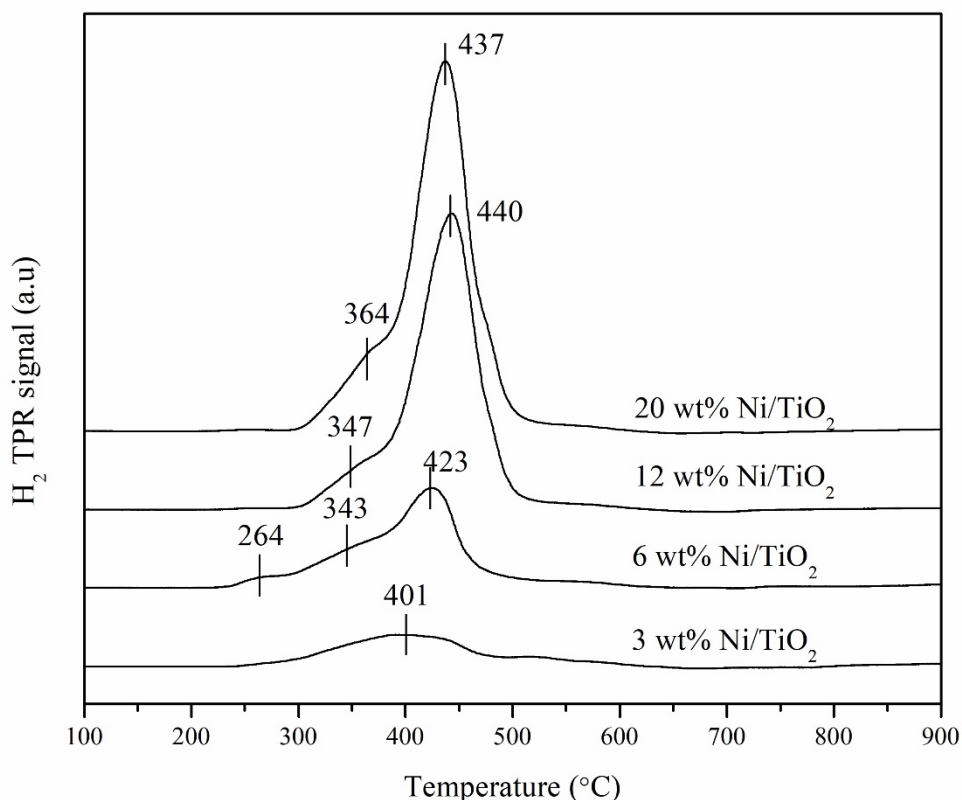
490

491

### 3.3.3 H<sub>2</sub> Temperature Program Reduction (H<sub>2</sub>-TPR) and H<sub>2</sub> chemisorption

H<sub>2</sub> Temperature Program Reduction (H<sub>2</sub>-TPR) is attributed to the interaction of metal active site and support. Figure 12 demonstrates the TPR profiles of 3, 6, 12 and 20wt% Ni-loaded TiO<sub>2</sub> catalysts. The reduction peaks were observed in the range of 250-450 °C which were assigned as conversion of Ni<sup>2+</sup> to Ni<sup>0</sup> on surface which interacted with TiO<sub>2</sub> support [30,31]. The different reduction temperature of NiO was attributed to different degree of interaction between NiO and TiO<sub>2</sub> support. This behavior depended on the preparation method and calcination temperature since these factors caused a different NiO dispersion state, NiO sizes and degree of interaction with TiO<sub>2</sub> and thus resulted in different reducibility of NiO particles. The shifting of NiO reduction peaks to higher temperature were observed upon increasing of Ni content which indicated to high dispersion of NiO species with stronger interaction with TiO<sub>2</sub> support [32]. Moreover, H<sub>2</sub> consumption considerably enhanced with the increase of Ni additions as follows: 3 < 6 < 12 < 20wt% Ni/TiO<sub>2</sub> as shown in Table 3. The signal of H<sub>2</sub>-TPR is referred to the amount of H<sub>2</sub> consumption, i.e., more intense of reduction peak implies to high H<sub>2</sub> consumption to reduce the metal in a catalyst. It was clearly seen that H<sub>2</sub> consumption was related to amount of NiO phase reduction to Ni metal; 20wt% Ni-modified TiO<sub>2</sub> provided 76.2 mmol/g of H<sub>2</sub> which was 5.5 times higher than H<sub>2</sub> consumption of 3wt% Ni-modified TiO<sub>2</sub>.

In order to validate the exposed NiO and/or Ni active species on catalyst surface, H<sub>2</sub>-chemisorption experiment was conducted. Due to H<sub>2</sub> favor to adsorb on metal active site, thus higher amount of H<sub>2</sub> chemisorbed can indicate to higher amount of metal active site. Table 3 illustrates the amount of H<sub>2</sub> chemisorbed of all catalysts. It is seen that the H<sub>2</sub> chemisorbed amount was increased with increasing of Ni loading on catalyst surface which corresponded to higher area of Ni adsorption sites for H<sub>2</sub>. Since H<sub>2</sub> is one of the reactants for CO<sub>2</sub> methanation, thus the results of H<sub>2</sub> chemisorption was related to enhance of catalytic activities of Ni-loaded catalysts which will be discussed in the latter part.



518 **Figure 12** H<sub>2</sub> TPR profiles of TiO<sub>2</sub>, 3, 6, 12 and 20wt% Ni-loaded TiO<sub>2</sub>.

### 519 **3.3 X-ray Absorption Spectroscopy analysis**

520 From catalytic activities results, it was found that addition of Ni into TiO<sub>2</sub> lattice  
 521 led to structural, physical and redox properties changing which also evidenced the altering of  
 522 catalytic activities performance. In this part, X-ray Absorption Spectroscopy (XAS) was used  
 523 to investigate the electronic state changing of Ni and Ti in freshly prepared catalysts and  
 524 monitor the changing of the catalysts during CO<sub>2</sub> methanation. The changing of catalysts  
 525 properties was studied by using data analysis of two regions; X-ray Absorption Near Edge  
 526 Structure (XANES) and Extended X-ray Absorption Fine Structure (EXAFS). All of data  
 527 reduction from XAS can be used to understand and describe the effect of Ni addition into TiO<sub>2</sub>  
 528 in improving CO<sub>2</sub> methanation.

#### 529 **3.3.1 X-ray Absorption Near Edge Structure (XANES) for monitoring Ni** 530 **and Ti oxidation states**

531 This part is divided into two parts; 1) ex-situ XANES analysis for freshly  
 532 synthesized catalyst and 2) in-situ XANES analysis for monitoring Ni and Ti oxidation state  
 533 during CO<sub>2</sub> methanation.

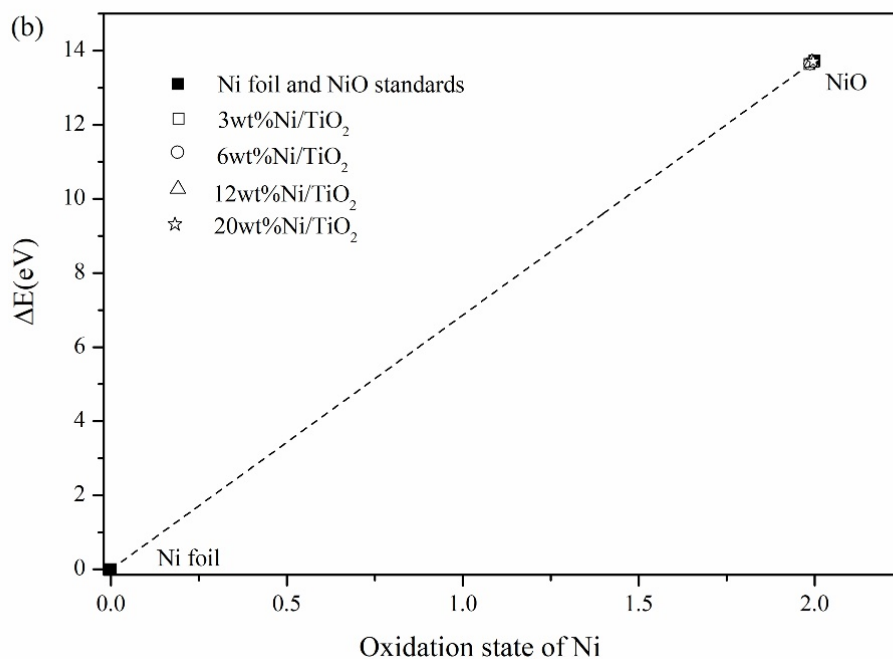
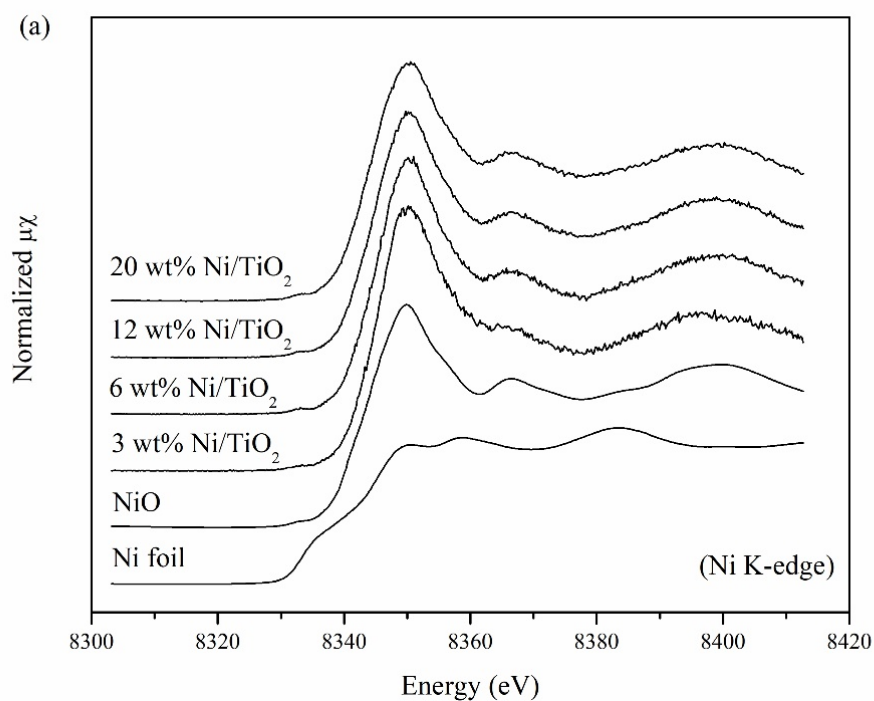
534 Figure 13(a) illustrates Ni K-edge XANES spectra of all freshly prepared  
535 Ni-loaded TiO<sub>2</sub> catalysts compared with Ni foil and NiO standards. The Ni foil spectrum  
536 exhibits an edge energy at around 8333 eV which is attributed to the electron transition from  
537 1s to 3d orbital [33]. For NiO standard, the white line peak at 8347 eV was observed which  
538 corresponded to multiple scattering process in octahedral NiO [33,34]. The oxidation state of  
539 probe atom can be initially estimated by comparing with the standard XANES spectra with  
540 certain oxidation state. From Figure 13(a), the Ni XANES spectra of Ni-loaded samples were  
541 almost identical to NiO standard spectrum which indicated to oxidation state of Ni-loaded TiO<sub>2</sub>  
542 in all samples were 2+. Moreover, in order to elucidate the oxidation state of Ni, the relationship  
543 between  $\Delta E$  (different of edge energy relative with Ni foil) and oxidation state of Ni was  
544 constructed. The edge energy of all samples can be obtained by taking the first derivative of  
545 those spectra and the turning point was assigned as an edge energy. Figure 13(b) displays the  
546 relationship between  $\Delta E$  and oxidation states of Ni for all Ni-loaded samples compared with  
547 two Ni standards. It can be seen that the apparent oxidation states of Ni for all Ni-loaded  
548 samples were 2+. Normalized Ti K-edge XANES spectra of all fresh as-synthesized samples  
549 display in Figure 14. Characteristic peaks of TiO<sub>2</sub> support and Ni-loaded samples were marked  
550 as pre-edge peaks A<sub>1</sub>–A<sub>3</sub> and B, a shoulder peak as C and a white line peak as D as shown in  
551 Figure 14(a) [35]. The first pre-edge peak (A<sub>1</sub>) was corresponding to a quadrupole transition to  
552 3d (*t<sub>2g</sub>*) state of the TiO<sub>6</sub> octahedron while that of A<sub>3</sub> and B peaks were assigned as dipole  
553 transition from 1s to hybridized p-d state of *t<sub>2g</sub>* and *e<sub>g</sub>*, respectively. The A<sub>2</sub> was not noticed in  
554 the larger size of anatase and rutile TiO<sub>2</sub>, but this peak appeared in the case of the small sized  
555 nanostructures [36]. The shoulder C was noted as transition shakedown process while that of  
556 D was assigned as transition of 1s to out-of-plane 4p<sub>z</sub> orbital [37]. The structures of all fresh  
557 samples were detected as anatase TiO<sub>2</sub> structure with consisted of Ti<sup>4+</sup> surrounding with six-  
558 fold coordinate which were related to XRD results. It is known that formation of oxygen  
559 vacancies within TiO<sub>2</sub> lattice lead to change of Ti<sup>4+</sup> oxidation state to Ti<sup>3+</sup> and distortion in the  
560 local TiO<sub>6</sub> octahedral coordination [38]. In the first change, the changing of Ti<sup>4+</sup> oxidation state  
561 to Ti<sup>3+</sup> was not observed from our results which might be due to small amount of metal addition  
562 when comparing with bulk TiO<sub>2</sub> concentration, thus, the changing of Ti<sup>3+</sup> was too small. On  
563 the other hand, the distortion in TiO<sub>2</sub> octahedral is caused from elongation or shortening of Ti–  
564 O bond length. Changing of Ti–O bond length lead to alteration of Ti 3d and O 2p density of  
565 state (DOS) and the changing of Ti–O orbital overlap results in changing the total DOS and its  
566 corresponding to electronic transition which reflected to the pre-edge feature [39]. The

567 changing of pre-edge feature is usually used to indicate the influence of metal substitution into  
568 host lattice. The pre-edge intensities were related to the symmetry of the crystal lattice, thus, a  
569 distortion and oxygen vacancies can cause an increase of pre-edge peaks [38-42]. Figure 14(b)  
570 shows Ti K-edge in the pre-edge region for TiO<sub>2</sub> and 3wt% Ni/TiO<sub>2</sub> and 20wt% Ni/TiO<sub>2</sub>. The  
571 pre-edge intensities increased with increasing of Ni content which was attributed to higher  
572 distortion and oxygen vacancies formation within TiO<sub>2</sub> lattice. This result can also confirm the  
573 substitution of Ni<sup>2+</sup> ions into Ti<sup>4+</sup> sites which led to oxygen vacancies formation and distortion  
574 of TiO<sub>2</sub> lattice. This phenomenon was in agreement with XRD and Ti EXAFS analysis for  
575 3wt% Ni/TiO<sub>2</sub> as discussed in the first part.

576 Second part is in-situ XANES analysis for monitoring Ni and Ti oxidation  
577 states during CO<sub>2</sub> methanation. In-situ Time-Resolved X-ray Absorption Spectroscopy (in-situ  
578 TR-XAS) was used to obtain the XANES results. 20wt% Ni/TiO<sub>2</sub> synthesized sample  
579 performed the highest CO<sub>2</sub> methanation activity, thus, this sample was selected to study by in-  
580 situ TR-XAS.

581 The original Ni oxidation state of freshly prepared Ni catalysts was +2  
582 which were confirmed by XANES results in previous part. In in-situ experiment, catalyst  
583 surface was cleaned up and reduced by using H<sub>2</sub> during heating from 50 to 450 °C as shown in  
584 Figure 15(a). During H<sub>2</sub> pretreatment, the characteristic peak of Ni species did not change in  
585 the temperature range from 50 to 340 °C. After that, the white line intensity of Ni<sup>2+</sup> (8347 eV)  
586 obviously decreased and then the feature of spectra was slightly changed with increase of  
587 pretreatment temperature and completely converted at 450 °C. After the temperature reached  
588 to 450 °C, the pretreatment temperature was hold at this point for 90 min to maintain metallic  
589 Ni active species before starting the reaction [43,44]. It indicated that the H<sub>2</sub> pretreatment  
590 process resulted in reduction of NiO to Ni<sup>0</sup>. Figure 15(b) shows in-situ TR-XAS results of  
591 20wt% Ni/TiO<sub>2</sub> during CO<sub>2</sub> methanation with H<sub>2</sub>/CO<sub>2</sub> ratio = 4 at reaction temperature range  
592 of 150 to 550 °C. The oxidation state of Ni remained unchanged during CO<sub>2</sub> methanation (Ni<sup>0</sup>)  
593 within the whole range of reaction temperature.

594 Figure 16(a) shows in-situ TR-XAS results of Ti K-edge for 20wt% Ni/TiO<sub>2</sub> over H<sub>2</sub>  
595 pretreatment condition at 50 to 450 °C. It can be seen that the spectra of 20wt% Ni/TiO<sub>2</sub> under  
596 pretreatment condition remained unchanged (Ti<sup>4+</sup>) and after conducting the CO<sub>2</sub> methanation,  
597 the oxidation state of Ti was still unchanged which can be observed by the same spectra feature  
598 of Ti K-edge for both pretreatment and reduction process (Figure 16(b)).

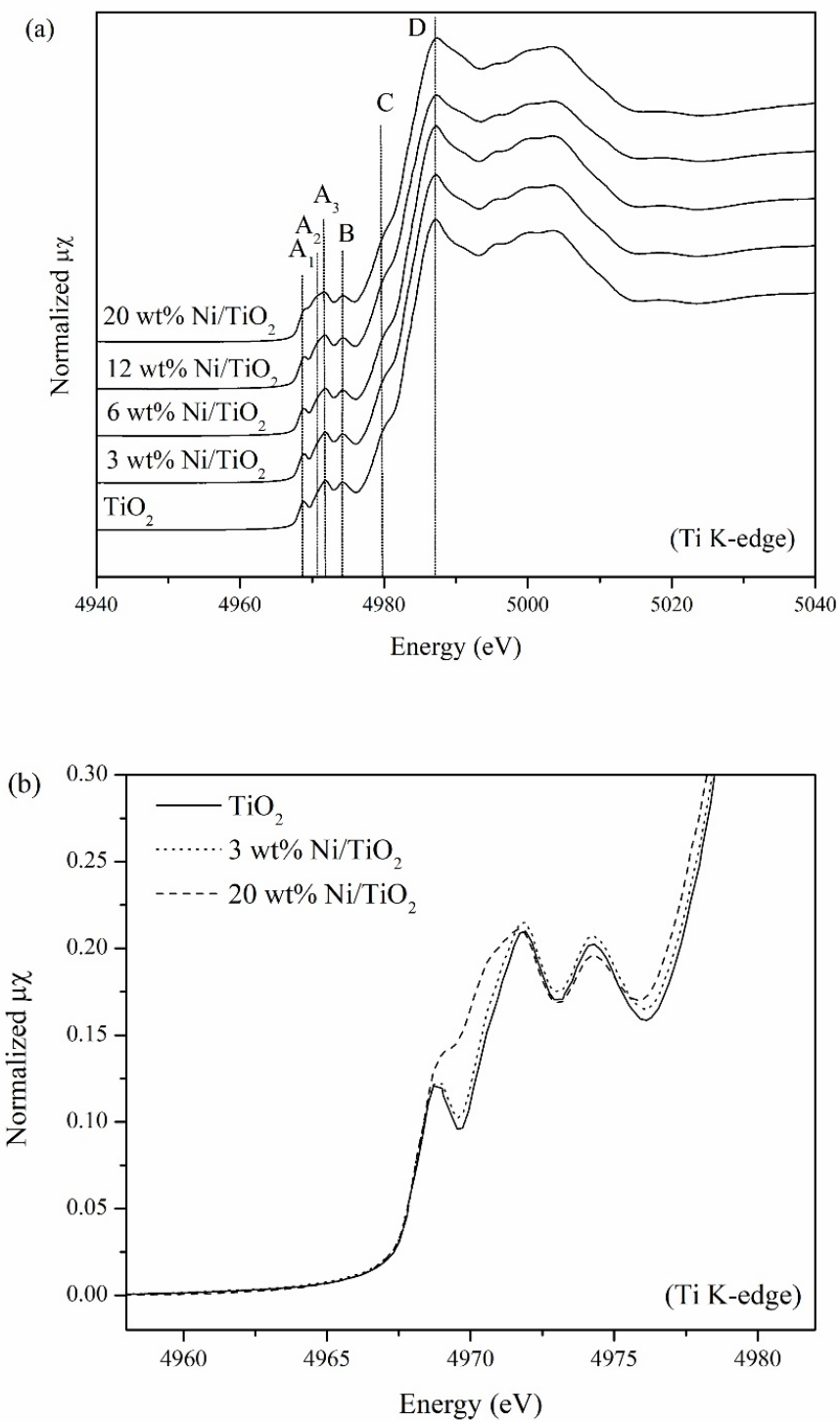


599 **Figure 13** (a) Normalized Ni K-edge XANES spectra of fresh samples (pure TiO<sub>2</sub>, 3, 6, 12  
600 and 20wt% Ni/TiO<sub>2</sub>) and references (NiO, Ni foil).

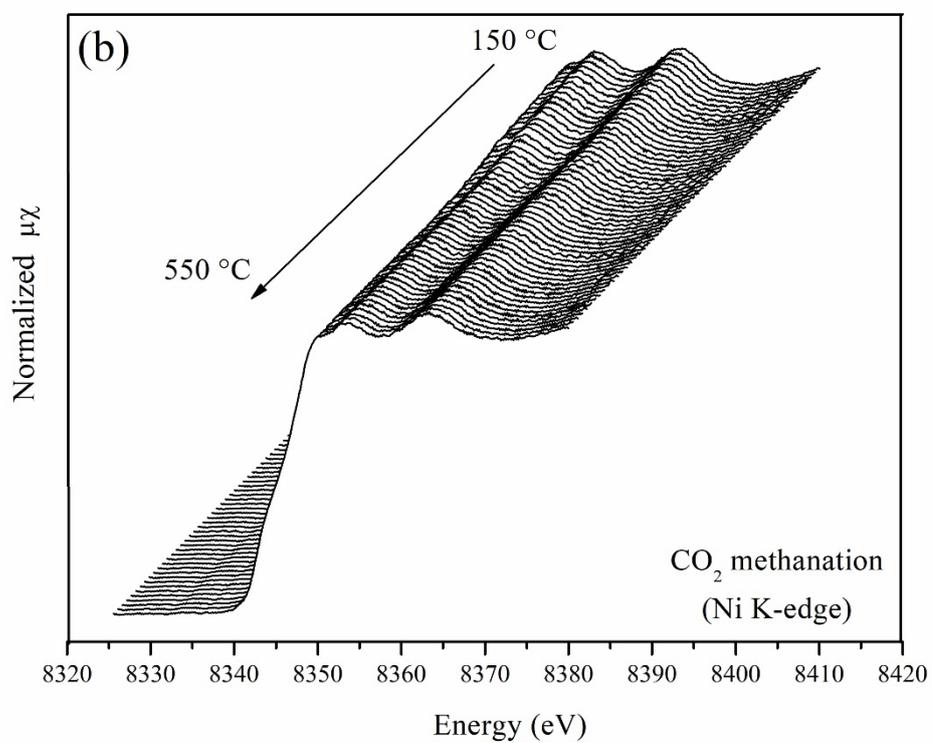
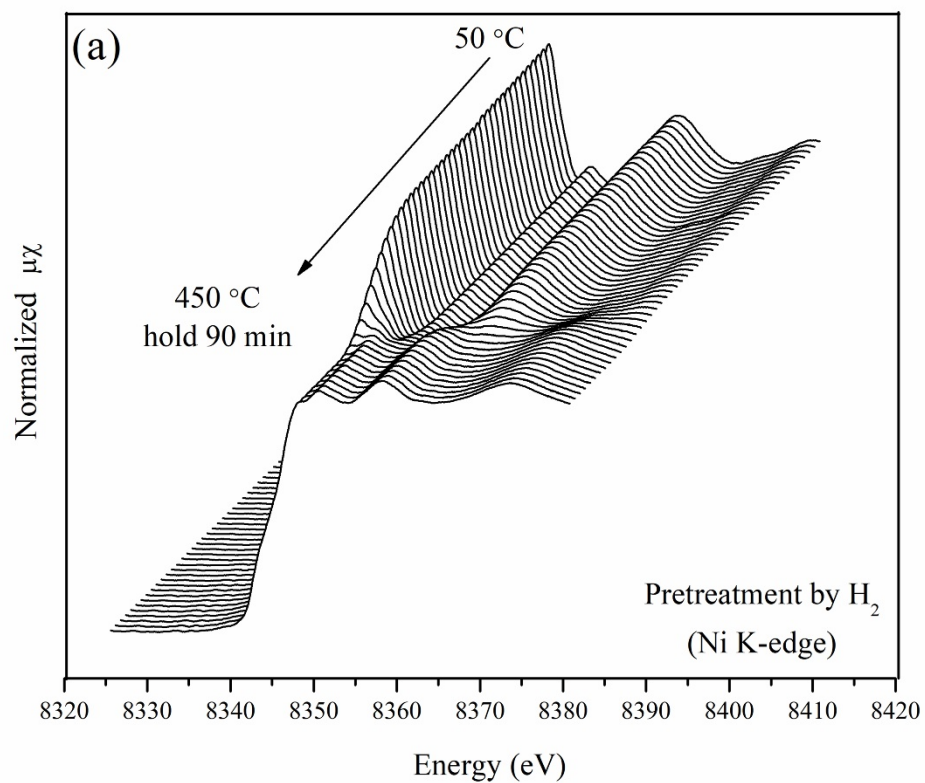
601 (b) Relationship between ΔE and oxidation state of Ni for determining the  
602 oxidation state of Ni in all synthesized catalysts.

603

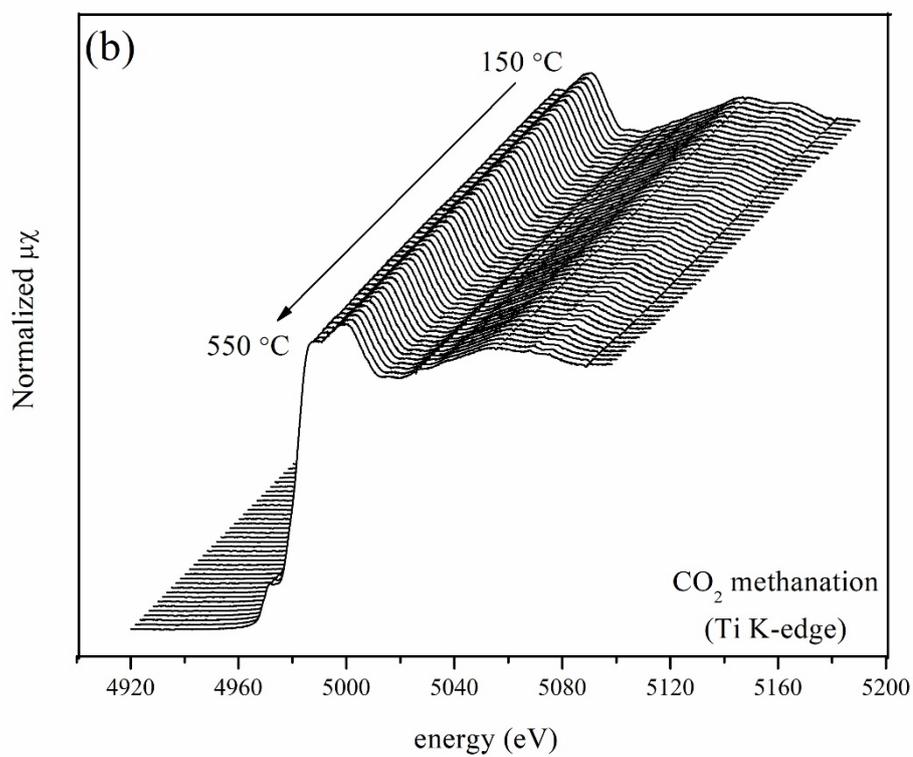
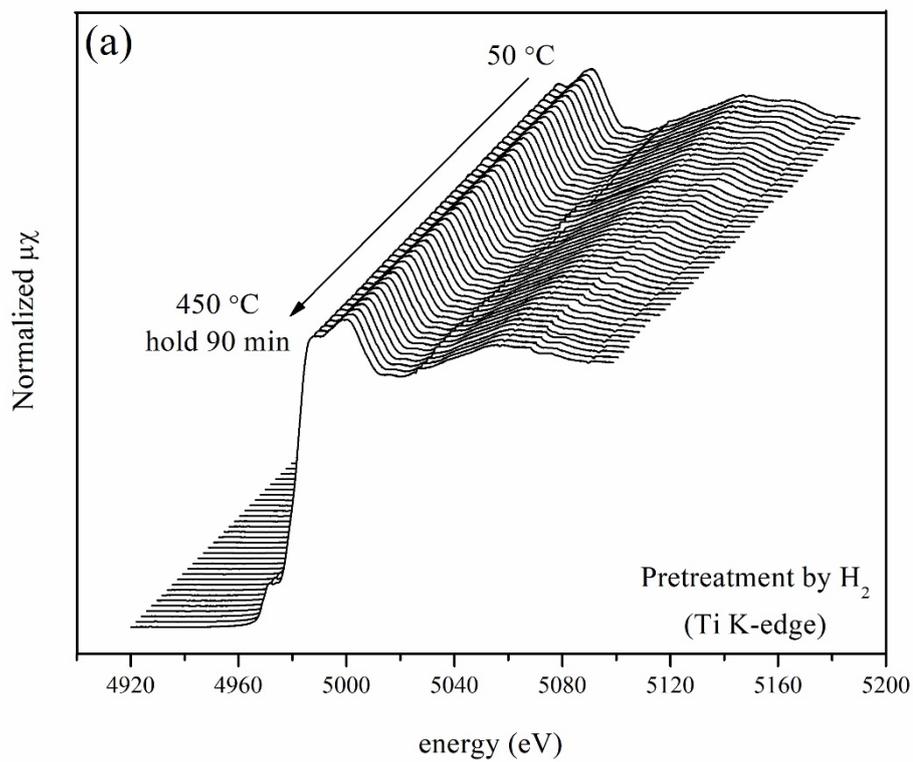
604



605 **Figure 14** (a) Normalized Ti K-edge XANES spectra of fresh samples (pure  $\text{TiO}_2$ , 3, 6,  
 606 12 and 20wt%  $\text{Ni/TiO}_2$ ).  
 607 (b) Ti K-edge XANES spectra in pre-edge region of  $\text{TiO}_2$ , 3wt%  $\text{Ni/TiO}_2$  and  
 608 20wt%  $\text{Ni/TiO}_2$ .



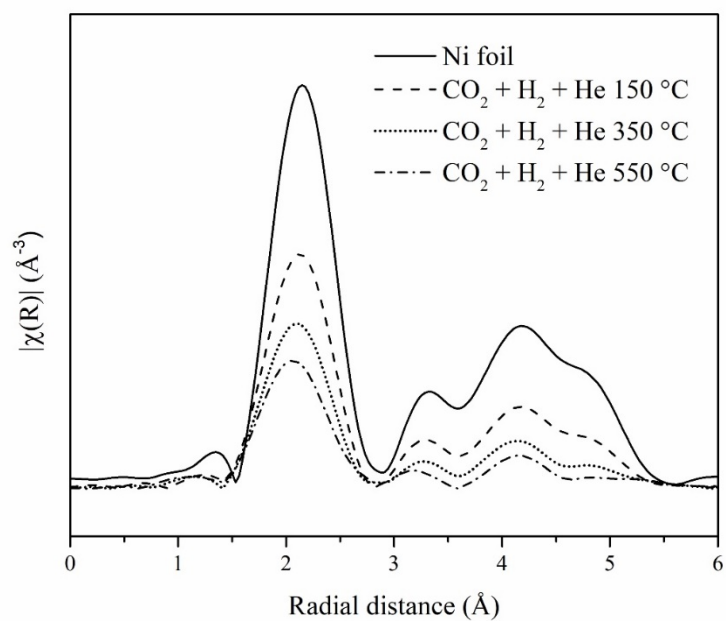
609 **Figure 15** in-situ Ni K-edge XANES spectra obtained from TR-XAS experiment of  
 610 20% wt Ni/TiO<sub>2</sub>: (a) pretreatment condition and (b) CO<sub>2</sub> methanation.



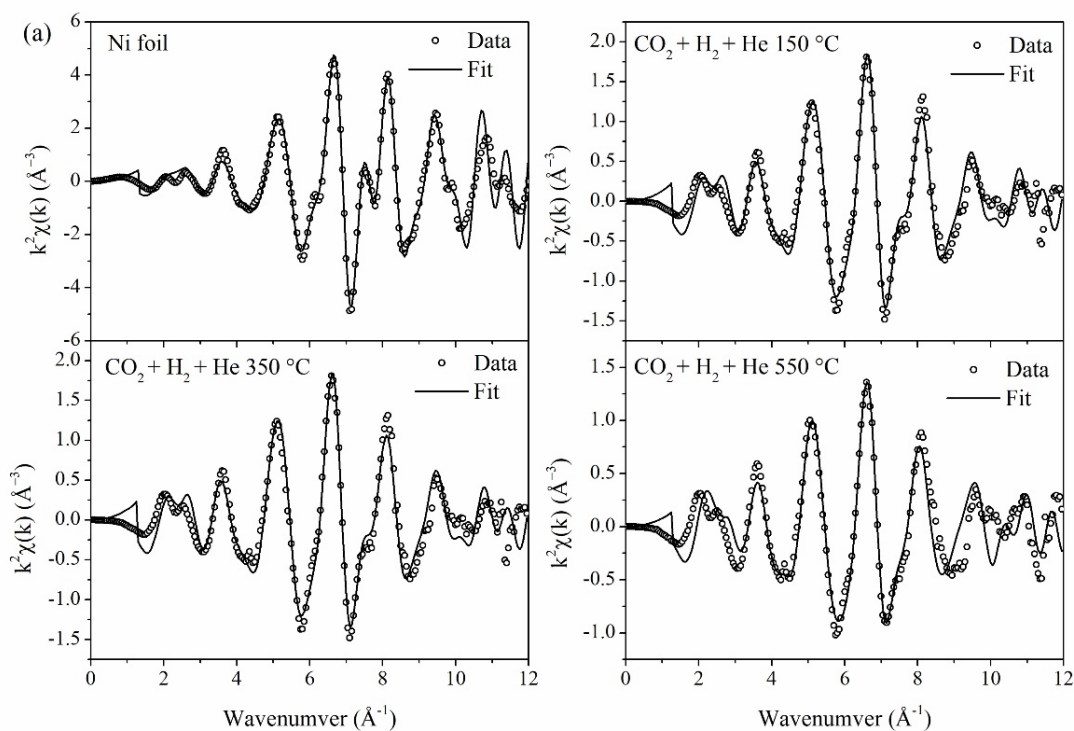
611 **Figure 16** in-situ Ti K-edge TR-XAS experiment of 20% wt Ni/TiO<sub>2</sub>: (a) pretreatment  
 612 condition and (b) CO<sub>2</sub> methanation.  
 613

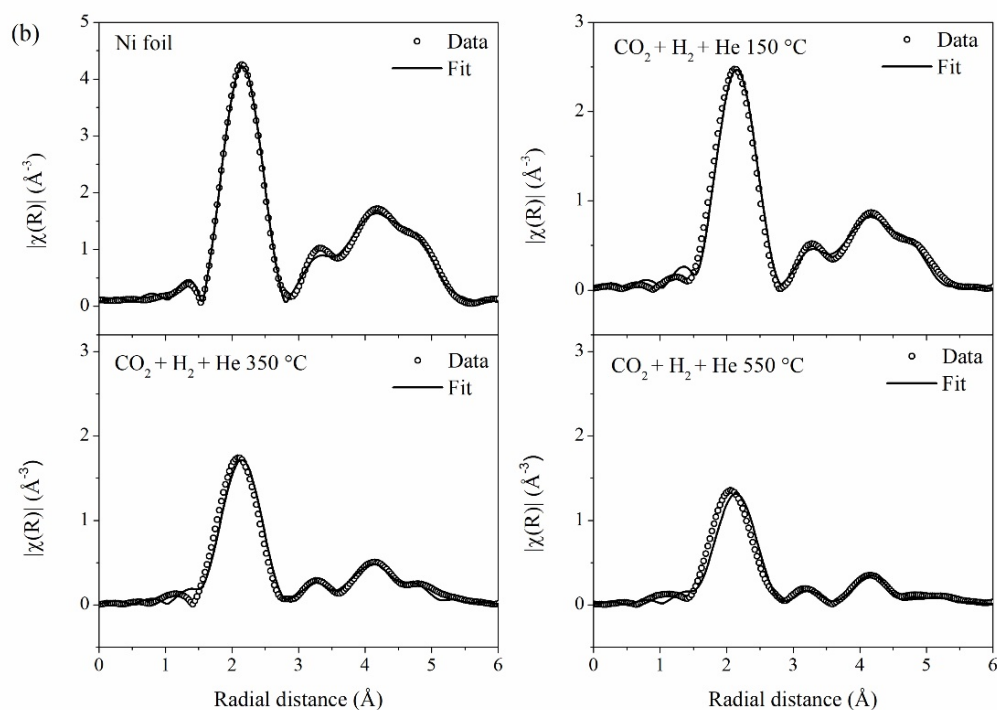
### 3.3.2 Extended X-ray absorption Fine Structure (EXAFS) study for monitoring Ni oxidation state during CO<sub>2</sub> methanation

Several works reported that Ni species on the catalyst surface is an important active site for enhancing CO<sub>2</sub> methanation rate since H<sub>2</sub> favors to adsorb on metal active site. Therefore, in this part, EXAFS analysis data was conducted to understand the state of Ni, structural changing of Ni during CO<sub>2</sub> methanation. The Fourier transformed function without phase correction of in-situ Ni K-edge EXAFS oscillation for 20wt% Ni/TiO<sub>2</sub> at the reaction temperature of 150, 350 and 550 °C is shown in Figure 17. The feature of all XANES spectra were similar to that of Ni foil. However, the amplitude of the spectra decreased with increased reaction temperature. Since, the amplitude is related to the coordination number around Ni probe atom, thus, EXAFS analysis can provide the information on the changing of Ni species during CO<sub>2</sub> methanation. The experimental data was normalized and the spectra were amplified by k<sup>2</sup> weight with R space window in the range of 1-5 Å and k range of 3-10 Å<sup>-1</sup>. Figure 18(a) and 18(b) displays the k<sup>2</sup> weight and the radial function of Ni K-edge EXAFS spectra for 20wt% Ni/TiO<sub>2</sub>, respectively. The calculated EXAFS of all catalysts were obtained by fitting with the cubic closed-packed (CCP) Ni structure. The best fitting analysis parameters are summarized in Table 4. The fitting results showed a first strongest peak at around 2.0 Å (2.48 Å from fitting) which assigned to a single scattering path of absorbing Ni atom with the nearest neighboring Ni atom (Ni–Ni). The calculated coordination number for Ni foil was 9.3 which indicated that Ni probe atom was surrounded by approximately 9 atoms. From Table 4, the calculated coordination number of 20wt% Ni/TiO<sub>2</sub> at 150, 350 and 550 °C were reduced to 7.6, 7.1 and 6.0, respectively. The lowering of coordination number of 20wt% Ni/TiO<sub>2</sub> with increasing of reaction temperature implied to higher level of unsaturated Ni–Ni coordination. High unsaturated of Ni–Ni coordination number can promote the dissociation of hydrogen on catalyst surface which can lead to high catalytic activity [45,46]. Therefore, high unsaturated Ni–Ni coordination number at high temperature (indicated by lowering of C.N.) provided high possibility of H<sub>2</sub> adsorption. However, the adsorption ability of H<sub>2</sub> on an active site was one of the factor to describe the catalytic performance. In order to describe the catalytic activities enhancement, understanding on the adsorption behavior of two reactants should be studied.



645 **Figure 17** Fourier Transform functions of *in-situ* EXAFS oscillation (without phase  
 646 collection) of Ni foil and 20wt% Ni/TiO<sub>2</sub> at 150, 350 and 550 °C under CO<sub>2</sub>  
 647 methanation.





648 **Figure 18** (a) The  $k^2$  weight EXAFS spectra of 20wt% Ni/TiO<sub>2</sub> at 150, 350 and 550 °C  
 649 under CO<sub>2</sub> methanation.  
 650 (b) The radial function of Ni K-edge EXAFS of 20wt% Ni/TiO<sub>2</sub> at 150, 350 and  
 651 550 °C under CO<sub>2</sub> methanation.

652  
 653 **Table 4** The best fitting parameters of 20wt% Ni/TiO<sub>2</sub>.

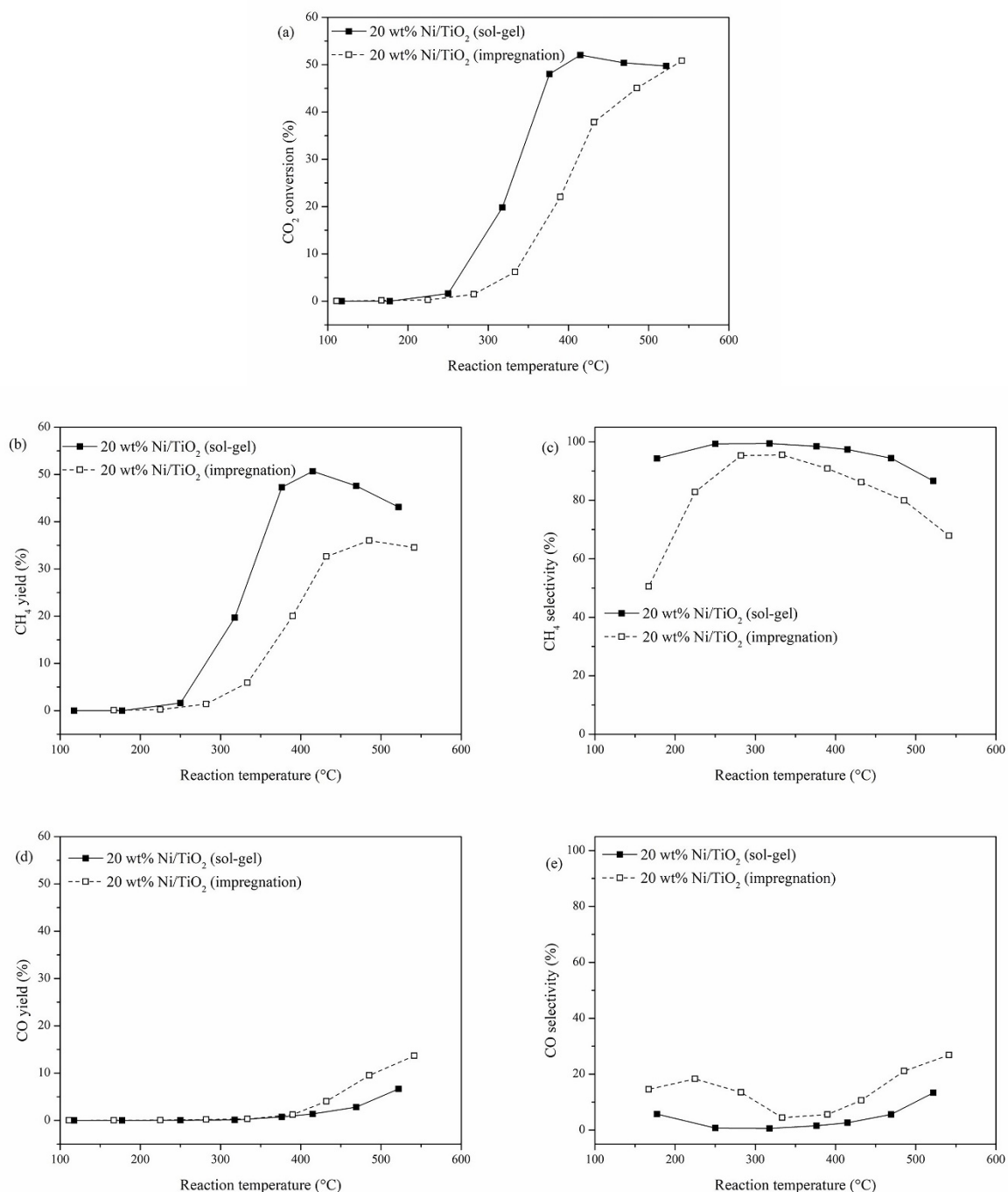
Samples	Shells	Best fit EXAFS parameters			
		N	$\sigma^2$	$\Delta E$ (eV)	R (Å)
Ni foil	Ni–Ni	9.3	0.0056	6.776	2.48
CO <sub>2</sub> + H <sub>2</sub> + He 150 °C	Ni–Ni	7.6	0.0088	6.417	2.48
CO <sub>2</sub> + H <sub>2</sub> + He 350 °C	Ni–Ni	7.1	0.0120	6.223	2.48
CO <sub>2</sub> + H <sub>2</sub> + He 550 °C	Ni–Ni	6.0	0.0130	6.240	2.48

654  
 655 **3.4 The role of added Ni on enhancing CO<sub>2</sub> methanation**  
 656 It has been reported that a different preparation method had a significant effect on  
 657 physical and chemical properties of the catalysts which can be altered to the catalytic activities.  
 658 In this work, sol-gel method was used to synthesize the catalyst for using in CO<sub>2</sub> methanation.

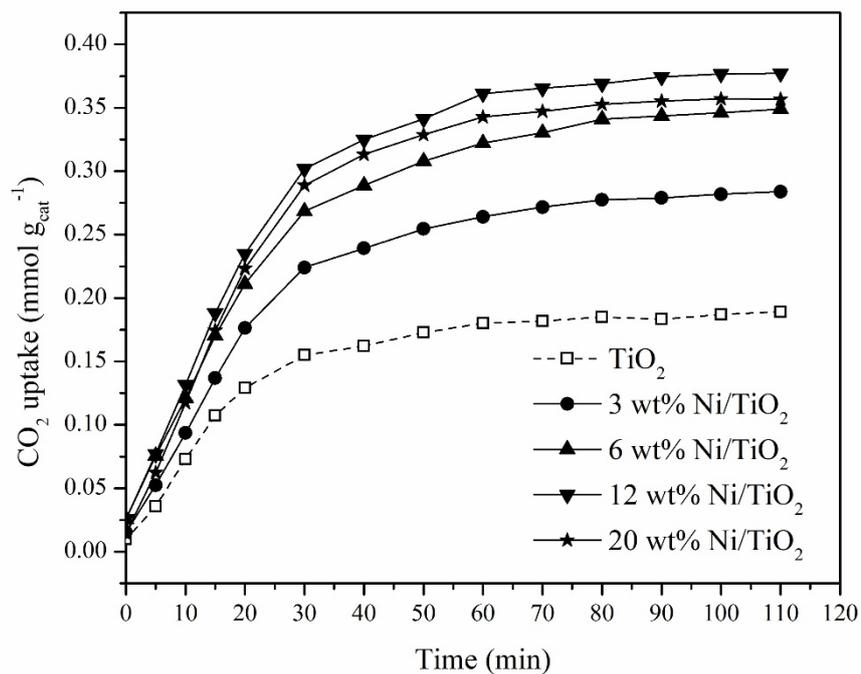
659 Since, this method is one of the reducible methods for preparing the catalyst, thus this method  
660 was employed. In the catalytic reaction, adsorption of the reactants on the catalyst surface is  
661 one of the most important elementary steps to control and dominate the catalytic reaction rate.  
662 Therefore, to speed up the reaction rate, enhancing the reactants adsorption ability on catalyst  
663 surface must be done. For CO<sub>2</sub> methanation, CO<sub>2</sub> and H<sub>2</sub> adsorption on catalyst surface can be  
664 enhanced by different approach. For CO<sub>2</sub> molecules, providing the basicity sites on the catalyst  
665 surface can increase the CO<sub>2</sub> adsorption capacity by acid-base interaction or existing of oxygen  
666 vacancy can also improve the adsorption capacity [47-49]. While H<sub>2</sub> molecules, it is known  
667 that H<sub>2</sub> favors to adsorb on metallic metal sites, especially on transition metals group, in  
668 dissociative form, thus dispersing of metal active sites on the catalyst surface can increase the  
669 H<sub>2</sub> adsorption capacity. Consequently, modification of the catalyst by above approaches would  
670 lead to increase of adsorption rate of reactants and also speed up the reaction rate. Preparation  
671 and modification by sol-gel method was used to alter the surface and catalyst properties which  
672 can provide both oxygen vacancies and metal active sites for CO<sub>2</sub> and H<sub>2</sub> adsorption,  
673 respectively. For CO<sub>2</sub> methanation, nickel was usually used to modify on support surface to  
674 increase the activity of the catalyst. In this work, added Ni on TiO<sub>2</sub> support acted as a bi-  
675 functional role in enhancing CO<sub>2</sub> methanation rate. First, addition of Ni during TiO<sub>2</sub> sol-gel  
676 process led to incorporation of Ni<sup>2+</sup> into TiO<sub>2</sub> lattice and resulted in strain and unbalanced  
677 charge and then oxygen vacancy was formed (this result can be evidenced by EXAFS data.).  
678 The oxygen vacancy was an active site for CO<sub>2</sub> adsorption; i.e., CO<sub>2</sub> interacted with oxygen  
679 vacancies by strong interaction and weakened the C=O bond [50,51]. Second, the excess  
680 amount of added Ni was existed in NiO form which might be located on the catalyst surface  
681 and this NiO phase was an active site for H<sub>2</sub> adsorption (after reduction to Ni<sup>0</sup> by pretreatment  
682 process before starting the reaction). Moreover, increasing of NiO crystallinity upon increase  
683 of Ni content was observed (increase of NiO peak intensity in XRD pattern) which resulted in  
684 lowering or inhibiting of TiO<sub>2</sub> crystal growth [52]. From this effect, smaller crystalline size of  
685 TiO<sub>2</sub> was occurred and higher surface area was observed. Figure 19(a)-19(c) illustrates the  
686 comparison of CO<sub>2</sub> methanation catalytic activities between 20wt% Ni/TiO<sub>2</sub> obtained by sol-  
687 gel and impregnation method. It is seen that addition of Ni into TiO<sub>2</sub> support by sol-gel method  
688 exhibited higher catalytic activity than that by impregnation method. Although, impregnation  
689 method is one of the simplest preparation method but the obtained catalyst properties were  
690 lowered, especially surface area and porosity which was an important properties that can  
691 dominate to the reduction rate. From Figure 19(d)-19(e), beside the higher catalytic activity of

692 catalyst obtained from sol-gel method, this catalyst was more selectively toward to CH<sub>4</sub> than  
693 CO while the impregnated catalyst exhibited an opposite result.

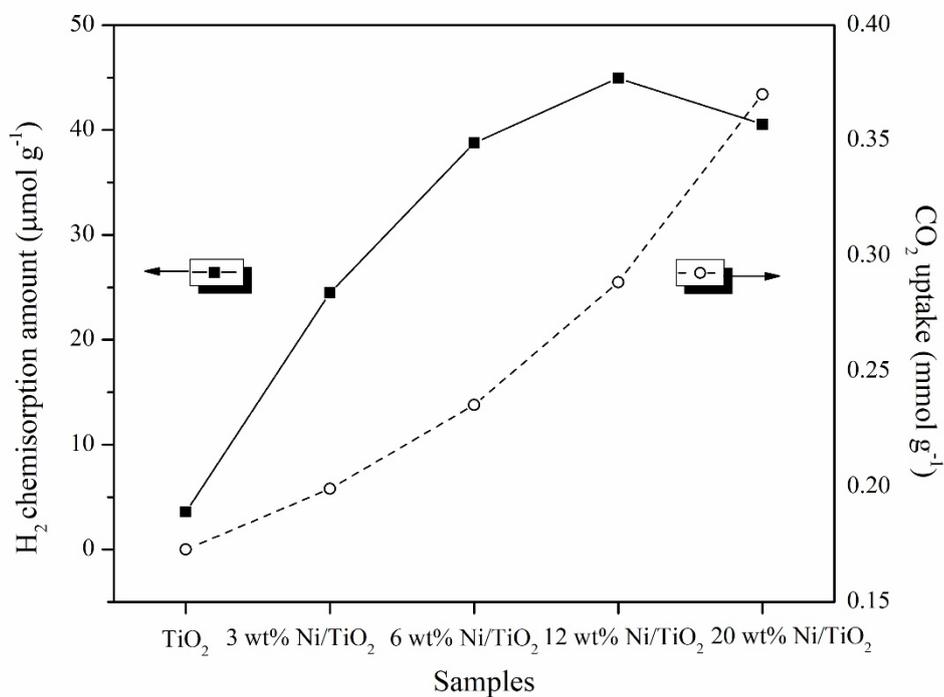
694 In order to evidence the role of added Ni in enhancing the reaction rate, CO<sub>2</sub> and  
695 H<sub>2</sub> adsorption studies were conducted. Since, in catalyst cycle, the adsorption of reactants on  
696 catalyst surface is usually assigned as a rate determining step, therefore, investigation of  
697 adsorption process can provide the information that can be used to understand and describe the  
698 role of catalyst in enhancing the reaction rate. For CO<sub>2</sub> methanation, increasing of CO<sub>2</sub> and H<sub>2</sub>  
699 adsorption can enhance the reaction rate, since, higher amount of adsorbed CO<sub>2</sub> and H<sub>2</sub> on  
700 catalyst surface would lead to more possibility to react and convert to products. In the case of  
701 H<sub>2</sub> adsorption, the results are illustrated in H<sub>2</sub>-chemisorption part and are summarized in Table  
702 3. It is assumed that only H<sub>2</sub> was adsorbed on Ni active site, thus higher amount of H<sub>2</sub>  
703 chemisorbed would be implied to higher Ni active area on catalyst surface. The results from  
704 Table 3 showed that H<sub>2</sub> chemisorption amount was increased with increasing of Ni content  
705 (5.80, 13.8, 25.5 and 43.4 μmol g<sup>-1</sup> for 3, 6, 12 and 20wt%, respectively). For CO<sub>2</sub> adsorption  
706 study, thermogravimetric analysis (TGA) was used. The CO<sub>2</sub> uptake experiment was conducted  
707 at 40 °C (the lowest temperature for the apparatus) and ambient pressure for 110 min. Figure  
708 20 illustrates the data reduction from TGA experiment which expressed in the term of CO<sub>2</sub>  
709 uptake at interval time. The results showed that the CO<sub>2</sub> uptake increased with time and almost  
710 constant within 60 min. The amount of CO<sub>2</sub> uptake was increased with Ni content (0.189, 0.248,  
711 0.349 and 0.377 mmol g<sup>-1</sup> for 0, 3, 6 and 12wt% Ni, respectively). The results from XRD and  
712 EXAFS indicated that added Ni<sup>2+</sup> was substituted into TiO<sub>2</sub> lattice and led to formation of  
713 oxygen vacancies which was reactive for CO<sub>2</sub> adsorption. However, increased Ni content up to  
714 20wt%, the CO<sub>2</sub> uptake was slightly dropped. This result can be used to relate with the highest  
715 catalytic activities of 20wt% Ni/TiO<sub>2</sub>. Since, the adsorption sites for CO<sub>2</sub> and H<sub>2</sub> were co-exist  
716 on the catalyst surface then if higher amount of adsorbed CO<sub>2</sub>, inhibition and suppression of  
717 H<sub>2</sub> adsorption on metal active site was probably occurred and then led to decrease of surface  
718 reaction between adsorbed CO<sub>2</sub> and H<sub>2</sub> and finally lower the catalytic activity. Therefore, an  
719 appropriate amount of adsorbed CO<sub>2</sub> and H<sub>2</sub> on catalyst surface would lead to high catalytic  
720 activities. Figure 21 shows the relationship between H<sub>2</sub> chemisorption and CO<sub>2</sub> uptake as a  
721 function of Ni content. It was found that 20wt% Ni/TiO<sub>2</sub> can maximize the CO<sub>2</sub> methanation  
722 rate. This result caused from the improvement of catalyst properties by addition of Ni which  
723 led to existence of active sites with appropriate performance to promote the CO<sub>2</sub> and H<sub>2</sub>  
724 adsorption.



725 **Figure 19** (a) CO<sub>2</sub> conversion, (b) CH<sub>4</sub> yield, (c) CH<sub>4</sub> selectivity, (d) CO yield and (e) CO  
 726 selectivity of 20wt% Ni-loaded TiO<sub>2</sub> by preparing with different preparation  
 727 methods; sol-gel and impregnation. The H<sub>2</sub>/CO<sub>2</sub>/He ratio was 24:6:10, total flow  
 728 rate was 40 mL min<sup>-1</sup> and WHSV was 48,000 mL g<sup>-1</sup> h<sup>-1</sup> at reaction temperature  
 729 100-550 °C.



730 **Figure 20** CO<sub>2</sub> uptake from TGA experiment for 0, 3, 6, 12 and 20wt% Ni/TiO<sub>2</sub>.



731 **Figure 21** The relationship between H<sub>2</sub> chemisorption and CO<sub>2</sub> uptake as a function of Ni  
732 content.

733

#### 734 4. Conclusion

735 In this work, the role of added Ni into TiO<sub>2</sub> support in enhancing CO<sub>2</sub> methanation rate  
736 was studied. The Ni supported TiO<sub>2</sub> with different amount of Ni loading as 3, 6, 12 and 20wt%  
737 Ni were synthesized by sol-gel method. The preparation method by addition of Ni during TiO<sub>2</sub>  
738 sol-gel process led to structural and surface properties changing which could alter to their  
739 catalytic activities. The results show that added Ni modified the catalyst properties in 2 ways;  
740 i) Ni<sup>2+</sup> was substituted into TiO<sub>2</sub> lattice which led to strain and unbalanced charge and then  
741 creating the oxygen vacancy. This effect can be evidenced by the results from distortion of Ti–  
742 O, Ti–Ti bond length (EXAFS analysis) and the enlargement of TiO<sub>2</sub> unit cell (XRD results).  
743 ii) upon increasing of Ni content, the excess amount of Ni was presented in NiO formed and  
744 probably located on the catalyst surface. This can be seen from the diffraction peak of NiO in  
745 XRD pattern. Moreover, the crystallinity of NiO increased with increasing Ni content which  
746 could inhibit to TiO<sub>2</sub> crystal growth and resulted in smaller TiO<sub>2</sub> crystalline sizes and then  
747 higher surface area was occurred. The existence of oxygen vacancy and NiO phase can be  
748 evidenced by XANES linear combination analysis. The results showed that NiO phase was  
749 increased with increasing of Ni loading. These two species that produced from addition of Ni  
750 during TiO<sub>2</sub> sol-gel process has a significant role in enhancing the CO<sub>2</sub> methanation rate. Both  
751 oxygen vacancy and NiO phase were an active site for promoting the adsorption of CO<sub>2</sub> and  
752 H<sub>2</sub> on catalyst surface, high possibility of surface reaction between these two adsorbed species  
753 were occurred and finally the reaction rate was enhanced. However, excess amount of adsorbed  
754 CO<sub>2</sub> on surface can inhibit the H<sub>2</sub> adsorption and lead to lowering of CO<sub>2</sub> rate.

#### 756 Acknowledgements

757 The authors gratefully acknowledge the facility support from Khon Kaen University,  
758 Institute for catalysis (Hokkaido University, Japan) for X-ray diffraction and N<sub>2</sub> adsorption-  
759 desorption analysis and Synchrotron Light Research Institute (Public Organization), Nakhon  
760 Ratchasima, Thailand for XAS analysis.

#### 761 Reference

- 762 [1] J. Gao, Y. Wang, Y. Ping, D. Hu, G. Xu, F. Gu, F. Su, RSC Adv. 2, (2012), 2358-2368.  
763 [2] W. Li, H. Wang, X. Jiang, J. Zhu, Z. Liu, X. Gao, C. Song, RSC Adv. 8, (2018), 7651-  
764 7669.  
765 [3] J. Gao, Q. Liu, F. Gu, B. Liu, Z. Zhong, F. Su, RSC Adv. 5, (2015), 22759-22776.

- 766 [4] M.S. Duyar, A. Ramachandran, C. Wang, R.J. Farrauto, J. *CO<sub>2</sub> Util.* 12, (2015), 27-33.
- 767 [5] D.C. Upham, A.R. Derk, S. Sharma, H. Metiu, E.W. McFarland, *Catal. Sci. Technol.* 5,  
768 (2015), 1783-1791.
- 769 [6] M. Schubert, S. Pokhrel, A. Thomé, V. Zielasek, T.M. Gesing, F. Roessner, L. Mädler,  
770 M. Bäumer, *Cat. Sci. Technol.* 6, (2016), 7449-7460.
- 771 [7] P. Panagiotopoulou, *Appl., Catal. A.* 542, (2017), 63-70.
- 772 [8] J. Gao, Q. Liu, F. Gu, B. Liu, Z. Zhong, F. Su, *RSC Adv.* 5, (2015), 22759-22776.
- 773 [9] H.C. Wu, Y.C. Chang, J.H. Wu, J.H. Lin, I.K. Lin, C.S. Chen, *Catal. Sci. Technol.* 5,  
774 (2015), 4154-4163.
- 775 [10] R. Zhou, N. Rui, Z. Fan, C.J. Liu, *Int. J. Hydrogen Energy.* 41, (2016), 22017-22025.
- 776 [11] J. Ashok, M.L. Ang, S. Kawi, *Catal. Today.* 281, (2017), 304-311.
- 777 [12] L.A.A. Varilla, N. Seriani, J.A. Montoya, *J. Mol. Model.* 25, (2019), 1-8.
- 778 [13] Y.X. Pan, C.J. Kia, D. Mei, Q. Ge, *Langmuir.* 26, (2010), 5551-5558.
- 779 [14] X. Li, Z.J. Zhao, L. Zeng, J. Zhao, H. Tian, S. Chen, K. Li, S. Sang, *J. Gong. Chem.*  
780 *Sci.*, 9, (2018), 3426-3437.
- 781 [15] B. Li, H. Metiu, *J. Phys. Chem.* 114, (2010), 12234-12244.
- 782 [16] X. Yan, Y. Liu, B. Zhao, Z. Wang, Y. Wang, C.J. Lia, *Int. J. Hydrogen Energy.* 38,  
783 (2013), 2283-2291.
- 784 [17] A. Niltrarach, S. Kityakarn, A. Worayingyong, J.T. Thienprasert, W. Klysubun, P.  
785 Songsiriritthigul, S. Limpijumnong. *Phys B Condens Matter.* 407, (2012), 2915-2918.
- 786 [18] X. Su, J. Xu, B. Liang, H. Duan, B. Hou, *J. Energy. Chem.* 25, (2016), 553-565.
- 787 [19] Q. Liu, J. Gao, F. Gu, X. Lu, Y. Liu, H. Li, Z. Zhong, B. Liu, G. Xu, F. Su, *J. Catal.* 326,  
788 (2015), 127-138.
- 789 [20] P. Kidkhunthod, *Adv. Nat. Sci. Nanosci. Nanotechnol.* 8 (2017).
- 790 [21] W. Klysubun, P. Kidkhunthod, P. Tarawarakarn, P. Sombunchoo, C. Kongmark, S.  
791 Limpijumnong, S. Rujirawat, R. Yimnirun, G. Tumcharern, K. Faungnawakij, J.  
792 *Synchrotron Radiat.* 24, (2017), 707-716.

- 793 [22] X. Gao, A. Traitangwong, M. Hu, C. Zuo, V. Meeyoo, Z. Peng, C. Li, *Energy Fuels*. 32,  
794 (2018), 3681-3689.
- 795 [23] V.R. Akshay, B. Arun, G. Mandal, M. Vasandhara, *Phys. Chem. Chem. Phys.* 21,  
796 (2019), 2519-2532.
- 797 [24] M. Manzoor, A. Rafiq, M. Ikram, M. Nafees, S. Ali, *Int. Nano Lett*, 8, (2018), 1-8.
- 798 [25] I. Ganesh, A.K. Kumar, P.P. Kumar, P.S.C. Sekhar, K. Radha, G. Padmanabham, G.  
799 Sundararajan, *Sci World J.* 2012, 2012, 13-20.
- 800 [26] P.M. Shirage, A.K. Rana, Y. Kumar, S. Sen, S.G. Leonardi, G. Neri, *RCS Adv.* 6,  
801 (2016), 82733-82742.
- 802 [27] K.C. Chanapatttharapol, S. Krachumram, Y. Poo-arporn, *Solid State Sci.* 99, (2020),  
803 106066.
- 804 [28] S. Tiwari, G. Bajpai, T. Srivastava, S. Viswakarma, P. Shirage, S. Sen, S. Biring, *Scr.*  
805 *Mater.* 129, (2017), 84-87.
- 806 [29] S.V. Moghaddam, M. Rezaei, F. Meshkani, R. Daroughegi, *Int. J. Hydrogen Energy.* 43,  
807 (2018), 16522-16533.
- 808 [30] J. van de Loosdrecht, A.M. van de Kraan, A.J. van Dillen, J.W. Geus, *J. Catal.* 170,  
809 (1997), 217-226.
- 810 [31] S.W. Ho, C.Y. Chu, S.G. Chen, *J. Catal.* 178, (1998), 34-48.
- 811 [32] J. Liu, C. Li, F. Weng, S. He, H. Chen, Y. Zhao, M. Wei, D.G. Evans, X. Duan, *Catal.*  
812 *Sci. Technol.* 3, (2013), 2627-2633.
- 813 [33] X. Meng, C. Wan, Y. Wang, X. Ju, *J. Alloys Comp.* 735, (2018), 1637-1647.
- 814 [34] K.I. Pandya, R.W. Hoffman, J. McBeen, W.E. O'Grady, *J. Electrochem. Soc.* 137, 1990,  
815 383-388.
- 816 [35] F. Farges, G.E. Brown Jr, J.J. Rehr, *Phys. Rev. B.* 56, (1997), 1809-1819.
- 817 [36] A. Sharma, M. Varshney, H.J. Shin, B.H. Lee, K.H. Chae, S. O. Won, *Mater. Chem.*  
818 *Phys.* 191, (2017), 129-144.
- 819 [37] J.H. Yang, H. Piao, A. Vinu, A.A. Elzatahty, S.M. Paek, J.H. Choy, *RCS, Adv.* 5,  
820 (2015), 8210-8215.

- 821 [38] B. Bharti, S. Kumar, H.N. Lee, R. Kumar, *Sci Rep*, 6, (2016), 1-12.
- 822 [39] M. Sahoo, A.K. Yadav, S. Ghosh, S.N. Jha, D. Bhattacharyya, T. Mathews, *Phys.*  
823 *Chem. Chem. Chem. Phys.* 21, (2019), 6198-6206.
- 824 [40] B.J. Hsieh, M.C. Tsai, C.J. Pan, W.N. Su, J. Rick, J.F. Lee, Y.W. Yang, B.J. Hwang,  
825 *NPG Asia Mat*, 9, (2017), e403.
- 826 [41] K. Huang, K. Sasaki, R.R. Adzic, Y. Xing, *J. Mater. Chem.* 22, (2012), 16824-16832.
- 827 [42] H. Song, T.G. Jeong, Y.H. Moon, H.W. Chun, K.Y. Chung, H.S. Kim, B.W. Cho, Y.T.  
828 Kim, *Sci. Rep.* 4, (2015), 1-8.
- 829 [43] L. Huang, L. Yan, M. Tang, G. Wang, Z. Qin, H. Ge, *ACS Omega*, 3, (2018), 18967-  
830 18975)
- 831 [44] J.A. Rodriguez, J.C. Hanson, A.I. Frenkel, J.Y. Kim, M. Pe´rez, *J. Am. Chem. Soc.*,  
832 124, (2002), 346-354.
- 833 [45] D. Hu, J. Gao, Y. Ping, L. Jia, P. Gunawan, Z. Zhong, G. Xu, F. Gu, F. Su, *Ind. Eng.*  
834 *Chem. Res.* 51, (2012), 4875-4886.
- 835 [46] P. van Helden, J.A. van den Berg, I.M. Ciobîˆcaˆ, *Catal. Sci. Technol.* 2, (2012) 491-  
836 494.
- 837 [47] W. Göpel, G. Rocker, R. Feierabend, *Phys. Rev. B.* 28, (1983), 3427-3438.
- 838 [48] J. Xu, X. Su, H. Duan, B. Hou, Q. Lin, X. Liu, X. Pan, G. Pei, H. Geng, Y. Huang, T.  
839 Zhang, *J. Catal.* 333, (2016), 227-237.
- 840 [49] X. Jia, X. Zhang, N. Rui, X. Hu, C. Liu, *Appl. Catal. B Environ.* 244, (2019), 159-169.
- 841 [50] F. Wang, S. He, H. Chen, B. Wang, L. Zheng, M. Wei, D.G. Evans, X. Duan, *J. Am.*  
842 *Chem. Soc.* 138, (2016), 6298-6305.
- 843 [51] M.Y.S. Hamid, M.L. Firmansyah, S. Triwahyono, A.A. Jalil, R.R. Mukti, E.  
844 Febriyanti, V. Suendo, H.D. Setiabudi, M. Mohamed, W. Nabgan, *Appl. Catal. A.* 532,  
845 (2017), 86-94.
- 846 [52] M. Pudukudy, Z. Yaakob, A. Kadier, M.S. Takriff, N.S.M. Hassan, *Int. J. Hydrogen*  
847 *Energy.* 42, (2017), 16495-16513.